Supporting Information

Inverse bimetallic RuSn catalyst for selective carboxylic acid reduction

Vassili Vorotnikov[=1], Todd R. Eaton[=1], Amy E. Settle[1], Kellene Orton[1], Evan C. Wegener[2], Ce Yang[3], Jeffrey T. Miller[2,3], Gregg T. Beckham[1]* and Derek R. Vardon[1]*

[1]National Bioenergy Center, National Renewable Energy Laboratory, Golden, Colorado, USA. [2]Davidson School of Chemical Engineering, Purdue University, West Lafayette, Indiana, USA. [3]Chemical Sciences and Engineering Division, Argonne National Laboratory, Argonne, Illinois, USA. [=]authors contributed equally to this work.
For correspondence email *gregg.beckham@nrel.gov **derek.vardon@nrel.gov

Catalyst synthesis, activity, and selectivity

Previous work identified RuSn as an outstanding catalyst in succinic acid hydrogenation when synthesized via sequential loading of Ru and Sn with a 1:1 molar ratio.[1] Highly dispersed nanoparticles of Ru were deposited via strong electrostatic adsorption (SEA) and reduction of a Ru^{3+} precursor, followed by Sn deposition via incipient wetness impregnation and reduction. To briefly summarize the synthetic method, metals were loaded onto nitric acid treated Darco activated carbon supports. Hexamine ruthenium chloride was used as the Ru precursor that was loaded by SEA at pH 11.5-12.0 to deprotonate the acidic carbon support. The Ru catalyst was then vacuum filtered, dried, and reduced at 300°C in pure flowing H_2 at 200 sccm for 4 hours. The metal loading procedure was repeated until the filtrate appeared colorless. Sn was then loaded by incipient wetness using tin(II) chloride dissolved in action. The catalyst was then reduced at 450°C in pure flowing H_2 at 200 sccm for 2 hours. Further details on the synthesis method can be found in the Supplemental Information of the initial paper.[1] This synthesis method resulted in the co-location of Ru with Sn and Sn oxide formation, as evidenced by microscopy and X-ray photoelectron spectroscopy (XPS).[1] This catalyst displayed higher yields for the target diol compared to the co-loading of Ru and Sn or sequential loading starting first with Sn. In this work, we used the same catalytic formulation for the hydrogenation of a simpler carboxylic acid, PA, which is more amenable to computational inquiry.

Batch reactor catalyst screening was initially used to confirm that the RuSn catalyst would also display high activity and selectivity for mono-carboxylic acid hydrogenation when compared to other bimetallic catalysts and their monometallic analogs, as shown in **Figure S1**. The results showed that monometallic catalysts were less reactive than the corresponding doped materials, evidenced by lower PA conversion and consistent with previous work with succinic acid.[1] Among the bimetallic catalysts tested, RuSn supported on powder activated carbon (PAC) was the most effective, yielding 71% 1-PrOH and 21% light products, including CO_2, methane, ethane, and propane. In comparison, PdRe-PAC and PtSn-PAC yielded only 28% and 42% 1-PrOH, respectively, when screened under these conditions.

Control reactions using Ru-PAC with 1-PrOH and propanal as reactants were performed to understand the production of light products. Both substrates showed similar yields: CO_2 (7-10%), methane (41-43%), ethane (47-49%), and propane (2%). These results suggest that propanal is easily hydrogenated over Ru-PAC, and related intermediates undergo subsequent cracking to C1 and C2 species. Product selectivities were comparable when starting with PA, 1-PrOH, and propanal, yet decarboxylation and decarbonylation pathways were indistinguishable, as water-gas-shift can readily occur in this sytem.[2] A detailed discussion of these results can be found below in **Figure S2**.

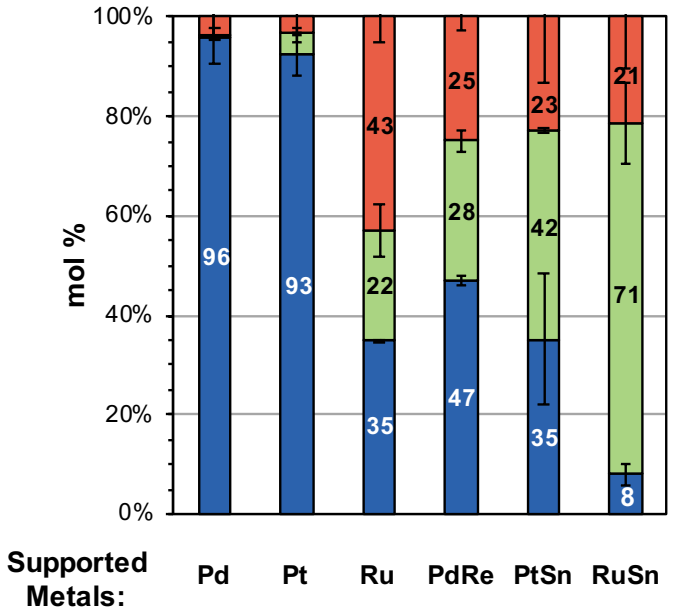

Figure S1. Catalyst screening results for propionic acid hydrogenation in batch reactors. Legend: propionic acid (blue), 1-propanol (green), and product loss not detected by HPLC (red). The percentage of each component is given by the overlaid number. Conditions: 160°C, 100 bar H_2, 20 mL of 25 g L^{-1} propionic acid, 100 mg catalyst, 15 hours. All batch catalysts are supported on powder activated carbon, with each metal loading at approximately 4 wt%.

Gas-phase hydrogenation products

The desired product from aqueous-phase hydrogenation of propionic acid, 1-propanol, remained in the condensed phase and was quantifiable by high pressure liquid chromatography (HPLC). However, for several catalysts there was a significant number of gas-phase products undetectable through HPLC. Qualitative sampling of the gas-phase products from propionic acid hydrogenation on Ru-PAC was performed to identify the undesired reaction products formed on Ru-PAC. Batch reactions were performed as described in the main text (e.g. ~0.1 g Ru-PAC, 100 bar H_2, 20 mL of 25 g L^{-1} substrate, 15 hours at 160°C), quenched and cooled to room temperature in a water bath, then slowly depressurized. During depressurization, 1-L gas bag samples were collected for gas chromatography analysis. The 1-L gas bags were directly hooked up to and analyzed by an Agilent 490 micro-GC with Molecular Sieve 5A, PoraPLOT Q, CP-Sil 5CB, and CP-Wax 52CB columns for H_2, CO, CO_2, and C1-C4 hydrocarbon detection. To determine potential reaction pathways, we also performed the batch reaction with 1-propanol and propanal as starting materials.

Liquid-phase reaction products for propionic acid, 1-propanol, and propanal hydrogenation are shown in **Figure S2A**. As shown in the main text, propionic acid hydrogenation on Ru-PAC yields only 22% 1-propanol, and 43% lights under these conditions. Lowering the pressure to 50 bar does little to change the conversion or product profile. Hydrogenation of 1-propanol yields 74% lights, with only 26% of the initial 1-propanol remaining in solution, suggesting that 1-propanol hydrogenation to lights occurs readily. Hydrogenation of propanal yields 94% lights, 5% 1-propanol, with only 1% of the initial propanal remaining. No propanal was detected from propionic acid hydrogenation. These results suggest that propanal hydrogenation to 1-propanol is very fast and that the initial hydrogenation of propionic acid is the rate limiting step in 1-propanol production. Analysis of the lights in each reactor is shown in **Figure S2B**. The carbon-containing products observed by micro-GC were CO_2, methane, ethane, and propane. Regardless of the reactant each of these products are synthesized, leading us to propose the reaction pathway in **Figure S3**.

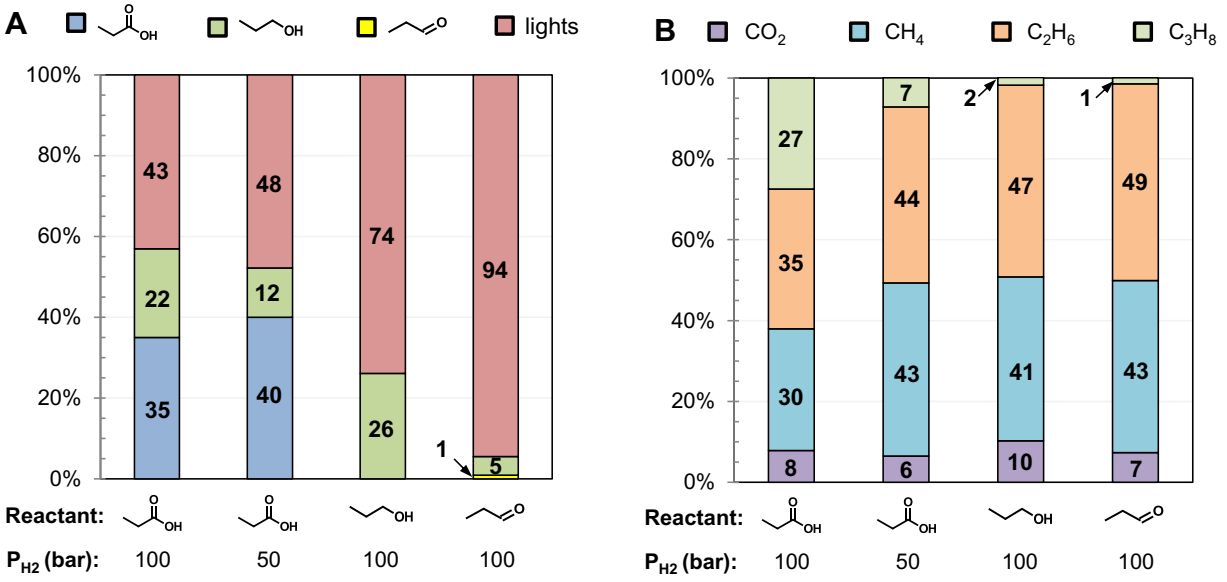

Figure S2. (A) Results from HPLC analysis of the liquid-phase reaction mixture, and (B) results from micro-GC analysis of the gas-phase "lights". Conditions: 0.1 g Ru-PAC, 160°C, 15 hours, 20 mL starting solution with 25 g L^{-1} reactant. The reactant and H_2 pressures are indicated below each figure.

The desired reaction pathway is shown in green in **Figure S3**, wherein propionic acid is hydrogenated to propanol, which is then further hydrogenated to 1-propanol. The lights observed for propionic acid, propanal, and 1-propanol hydrogenation are formed through undesired hydrogenation, decarbonylation, and decarboxylation reaction. Propane can be formed from 1-propanol hydrogenation. Methane can be formed from C-C scission of

propane, forming ethane as a byproduct. Ethane can be formed either from propanal decarbonylation or propionic acid decarboxylation. Although only CO_2 is observed in the gas-phase, it is difficult to assess from these results whether decarbonylation or decarboxylation is more likely, since CO can readily be oxidized to CO_2 through the water-gas-shift reaction, which has been shown to proceed over Ru catalysts and is likely under these conditions given the aqueous environment. However, computational results suggest that lower energy barriers exist for decarbonylation (see the main text). According to these results propane cracking to methane and ethane is more prevalent than decarbonylation or decarboxylation pathways, as can be seen by comparing CO_2 to methane concentrations.

Control reactions on Ru-PAC were performed with 1-PrOH and propanal as starting substrates to better understand the reaction pathways. Hydrogenation of 1-PrOH yielded 74 mol% lights with 26 mol% 1-PrOH remaining. Hydrogenation of propanal yielded 94 mol% lights, 5 mol% 1-PrOH, and 1 mol% propanal remaining. Lights analysis from these control reactions show approximately the same ratios of CO_2, methane, ethane, and propane. These results demonstrate that lights formation through propanal proceeds much faster than through 1-PrOH.The combined steps of 1-PrOH hydrogenation to propane and propane cracking to methane and ethane lead to the majority of undesired lights formation. Decarboxylation of PA to CO_2 and ethane, or decarbonylation of propanal to CO and ethane are minor reaction pathways for lights formation, though the two pathways are indistinguishable from current results. Although CO is not observed, water-gas-shift readily occurs over Ru in an aqueous reaction environment. When the reactions are run under milder conditions on Ru-PAC (140°C, 25 bar H_2, see SI), PA conversion was reduced to 33%, yet selectivity towards 1-PrOH and lights, ($S_{1\text{-PrOH}}$ = 30% , S_{lights} = 70%) did not significantly change from the standard conditions ($S_{1\text{-PrOH}}$ = 34%, S_{lights} = 66% at 160°C, 100 bar H_2). This shows that optimizing reaction conditions alone will not improve selectivity.

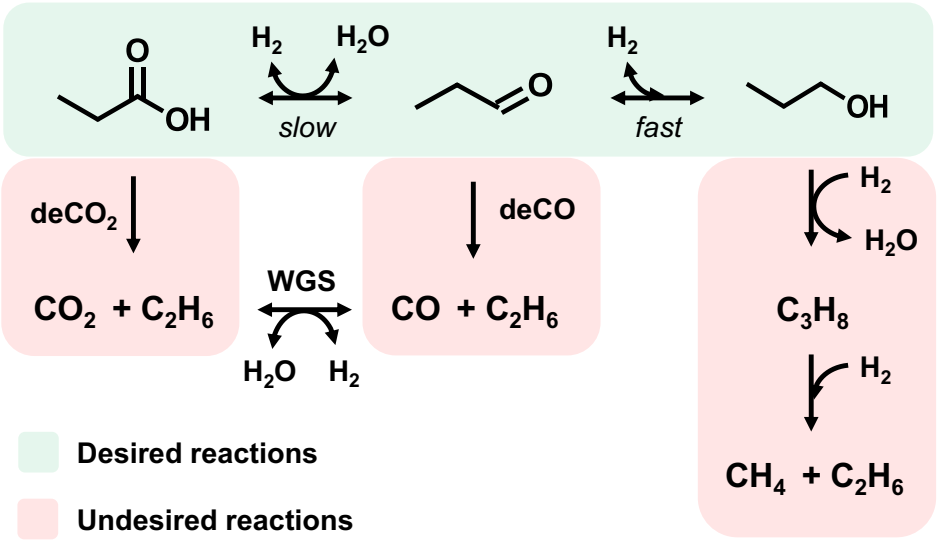

Figure S3. Proposed reaction pathway for propionic acid hydrogenation on Ru-PAC based on analysis of liquid- and gas-phase products.

Catalyst inhibition experiment

Experimental observations discussed in the main text indicate that co-feeding phenylphophonic acid (PPA) to the catalyst bed leads to reversible inhibition of RuSn-GAC but not Ru-GAC. Time on stream results for inhibition experiments are shown below in **Figure S4** for RuSn-GAC. As discussed in the main text, addition of PPA to the feed stream rapidly reduces the rate of propionic acid hydrogenation on RuSn-GAC, while having no effect on Ru-GAC. Removing PPA from the feed stream rapidly restores the catalytic activity on RuSn-GAC. This suggests that any P-O-Sn bonds formed during inhibition are reversible under hydrogenation conditions.

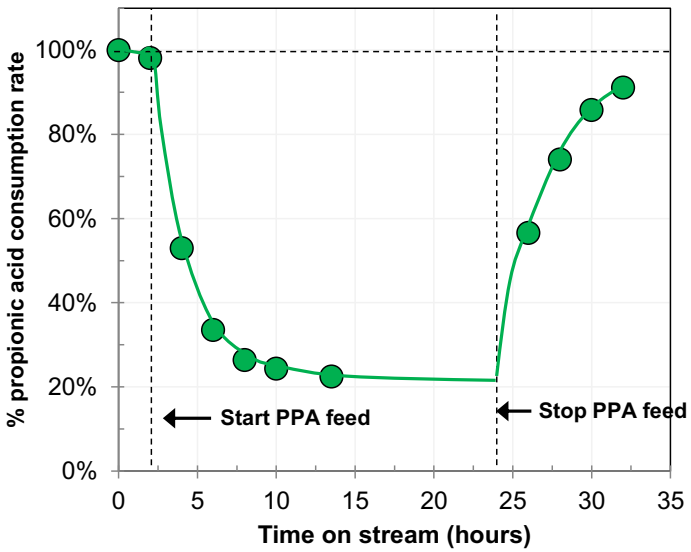

Figure S4. Reversible inhibition of RuSn-GAC with PPA during propionic acid hydrogenation. Conditions: 160°C, 200 sccm H_2, 100 bar H_2, propionic acid WHSV = 4 h^{-1}. PA feed solutions consist of 100 g L^{-1} PA and either 0 g L^{-1} or 2 g L^{-1} PPA.

X-ray absorption spectroscopy

X-ray absorption spectroscopy experiments were performed at the Materials Research Collaborative Access Team (MRCAT) and CMC beamlines of the Advanced Photon Source at Argonne National Laboratory. Powder catalyst samples were loaded as self-supporting wafers in a 6-sample stainless steel sample holder. For samples requiring pre-treatment, the sample holder itself was loaded in a quartz sample tube equipped with gas and thermocouple ports and sealed at both ends by Kapton windows. The samples were heat-treated to 160°C under flowing H_2 (4% H2/He at 100 sccm) in a tube furnace for 30 minutes, then cooled under flowing He (100 sccm) to room temperature, sealed, and then placed in the beamline for XAS spectra collection. The XAS spectra were collected in transmission mode at the Ru (22.1172 keV) and Sn K edges (29.2001 keV). The XAS data was fit using standard procedures based on WINXAS software, and k^2-weighted Fourier transform data was used to obtain the EXAFS coordination parameters with least-squares fits in q- and r-space of the isolated nearest neighbor.

Detailed results from analysis of both XANES and EXAFS spectral regions are given in **Table S1**. In addition to the information given in the main text, this table includes the Debye-Waller factor ($\Delta\sigma^2$) for the EXAFS fit and includes data for Ru and Sn standards. The Ru_3Sn_7 standard was synthesized according to a previously reported procedure. XANES spectra of some standards are shown in **Figure S5** and **Figure S6**, for Ru and Sn, respectively. In the spectra of Ru standards, the edge shifts to higher energy with increasing oxidation state, e.g., Ru^0 compared to Ru^{3+}. The shape of the XANES is determined by the energy of the empty valence orbitals and the allowed transitions. For Ru_3Sn_7 the edge energy is lower than that in metallic Ru and the leading-edge intensity (white line) is lower. These indicate Ru is more electron rich compared to metallic Ru. Therefore, the

shift to lower energy than metallic Ru and lower white line are characteristic of RuSn bimetallic formation. This energy shift is also observed for RuSn-PAC (as shown in the main text), though the RuSn-PAC and Ru_3Sn_7 spectra are otherwise very different, clearly indicating that RuSn-PAC does not form Ru_3Sn_7 alloy. For the spectra of Sn standards, the XANES energy and white line intensity increase as the oxidation state increases. The XANES spectrum of spent RuSn-PAC, without H_2 treatment, is identical to that of SnO_2, though the EXAFS shows that the Sn oxide domains on RuSn-PAC are small and have no long-range order.

Table S1. XAS results for Ru and Sn standards and catalysts.

Sample	Treatment	XANES Energy, keV	Scatter	N	R, Å	$\Delta\sigma^2$ (x 10^3)	Eo, eV	Est. Size (nm)
Ru Edge								
Ru Foil	Standard	22.1170	Ru-Ru	12	2.68	0.0	-1.0	
$Ru(NH_3)_6Cl_2$	Standard	22.1242						
$Ru(NH_3)_6Cl_3$	Standard	22.1274						
RuO_2	Standard	22.1294						
Ru_3Sn_7	Standard	22.1160						
Ru-PAC Fresh	Air, RT	22.1264	Ru-O	3.4	2.00	8.0	-2.3	Partially metallic
			Ru-Ru	5.3	2.68	4.0	-8.6	
Ru-PAC Spent	Air, RT	22.1280	Ru-O	5.8	2.00	8.0	-4.2	
RuSn-PAC Fresh	Air, RT	22.2183	Ru-O	5.5	2.00	8.0	-3.7	
RuSn-PAC Spent	Air, RT	22.1285	Ru-O	5.8	2.00	8.0	-4.3	
Ru-PAC Fresh	160°C H_2	22.1181	Ru-Ru	9.1	2.65	4.0	-1.6	4.0
Ru-PAC Spent	160°C H_2	22.1171	Ru-Ru	9.3	2.65	4.0	-0.9	4.0
RuSn-PAC Fresh	160°C H_2	22.1171	Ru-Ru	9.5	2.66	4.0	-2.3	4.5
RuSn-PAC Spent	160°C H_2	22.1172	Ru-Ru	7.1	2.65	4.0	-2.7	2.5
Sn Edge								
Sample	Treatment	XANES Energy, keV	Scatter	N	R, Å	$\Delta\sigma^2$ (x 10^3)	Eo, eV	Oxidation State
Sn Foil	Standard	29.2000						0
$SnCl_2$	Standard	29.1996						II
SnO	Standard	29.1999						II
SnO_2	Standard	29.2039	Sn-O	6	2.05	0.0	0.2	IV
RuSn-PAC Fresh	Air	29.2040	Sn-O	5.8	2.04	2.0	-1.1	IV
RuSn-PAC Spent	Air	29.2040	Sn-O	6	2.05	2.0	-0.7	IV
RuSn-PAC Fresh	160°C H_2	29.0010	Sn-O	2.5	2.06	5.0	1.1	II
RuSn-PAC Spent	160°C H_2	29.2000	Sn-O	1.9	2.05	5.0	-2.1	II

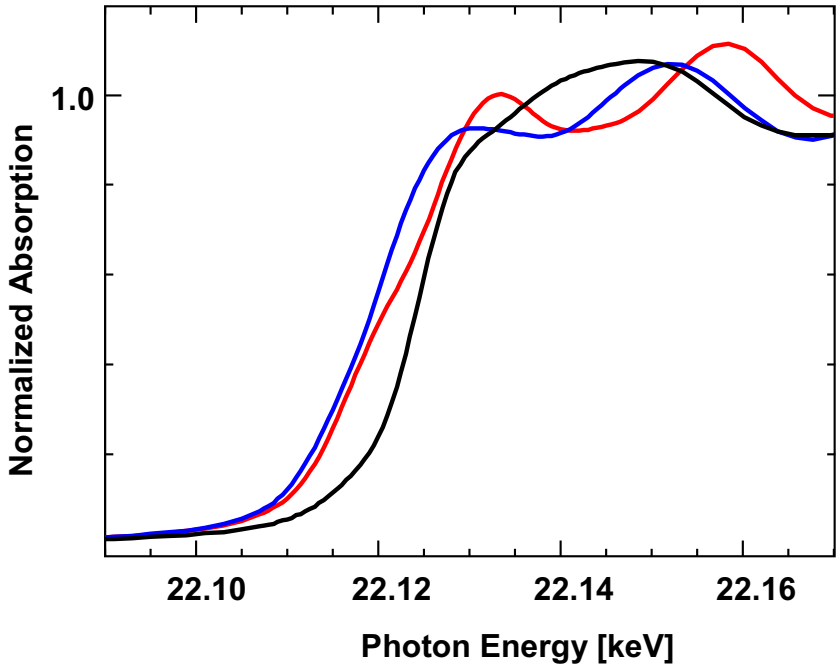

Figure S5. Ru K-edge XANES from 22.09 to 22.17 keV for Ru foil (red), Ru_3Sn_7 alloy (blue), and $RuCl_3$ (black).

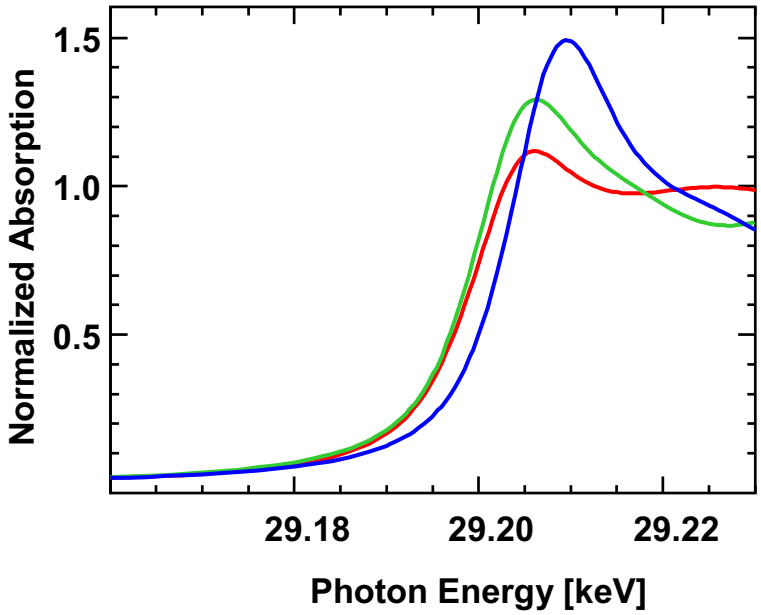

Figure S6. Sn XANES from 29.16 to 29.23 keV for Sn foil (red), SnO (green), and SnO_2 (blue).

Computational Modeling

Periodic density functional theory (DFT) calculations were carried out using Vienna *Ab initio* Simulation Package (VASP), version 5.4.4.[3-6] The ion-electron interactions were described using the PAW potentials.[7, 8] The electron-electron exchange and correlation energies were computed using Perdew, Burke, and Ernzerhof (PBE) functional.[9] The van der Waals (vdW) forces were calculated using the method of Tkatchenko and Scheffler (TS) as implemented in VASP.[10] The 19×19×13 and 15×15×11 Γ-centered *k*-meshes were used for bulk Ru and SnO calculations, respectively. Murnaghan-Birch equation of state was used to estimate bulk parameters, which were then confirmed to within 0.001 Å with single-point energy calculations.[11, 12] The resulting lattice parameters are in excellent agreement with previous experimental and DFT estimates.

Parameters specific to each model surface are shown in **Table S2**. For each surface, the *k*-point mesh (3×3×1), the energy cutoff (400 eV) and the vacuum layer (30 Å) were chosen such that the adsorption energy of representative species (or clusters) is converged to within 0.01 eV. A five-layer 4×4 surface was used to represent Ru(0001). Bimetallic Sn/Ru(0001) were constructed by replacing top layer Ru atoms with Sn at varying concentrations as shown in **Figure S7**. Subsurface Sn was found to be less stable and was therefore not considered in this work.[1] The bottom three layers were frozen in corresponding bulk-optimized positions while the top two layers were allowed to relax. We optimized a number of Sn_4O_4 clusters cleaved from bulk SnO on a 5×5 Ru(0001) to remove periodicity-induced interactions between the Sn_4O_4 cluster and propionic acid. For this SnO/Ru model, 3-layer Ru slab was used for computational efficiency, showing energy differences within ~0.01 eV of a 4-layer model. The minimum-energy stoichiometry-maintaining structure was then chosen to model small Ru-supported SnO particles, as shown in **Figure S7E**.

The relaxation was performed until all forces were lower than 0.01 eV $Å^{-1}$ using a conjugate-gradient algorithm. Dipole corrections were included in all calculations.[13, 14] Transition states were located using the climbing nudged elastic band (cNEB) method,[15] followed by the Dimer routine to ensure convergence to within 0.01 eV $Å^{-1}$.[16] All transition states were confirmed by the presence of a unique imaginary frequency along the investigated bond scission reaction.

For selective PA hydrogenation to 1-PrOH, transition states for each elementary step were computed explicitly using DFT. For non-selective routes, which comprise a vast number of elementary reactions, we used Brønsted-Evans-Polanyi (BEP) relations for crude estimates, followed by DFT refinement where applicable. Past efforts showed that structure- and reaction- specific BEP relations can reduce the computational cost, allowing for relatively accurate barrier estimates from less-demanding DFT-computed reaction energies.[17-20] Furthermore, only initial elementary steps typically end up rate-determining in the decomposition of oxygenates over Ru.[21-24] To mitigate the computational burden, we thus developed reaction-specific BEP relations by compiling DFT results from Ru-specific work on methanol,[23, 25] ethanol,[22, 26] hexadecanol,[21] C_1-C_4 aldehydes and ketones,[27, 28] acetic acid,[29, 30] propionic acid[24] and levulinic acid[31] (see **Tables S3-9** and **Figures S9-14**), and applied them to the over-reduction of 1-propanol and the initial steps leading to cracking. This methodology was applied to Ru, Sn/Ru and SnO/Ru models. The newly-developed O-H and C-H bond-specific BEP relations were used for SnO/Ru since they showed significant deviations from those developed for metallic surfaces.

Table S2. Model DFT surfaces and corresponding parameters. The number of atomic layers is shown.

Model surface	Layers (frozen)	Supercell	*k*-mesh
Ru(0001)	5 (3)	4×4	3×3×1
6% Sn/Ru(0001)	5 (3)	4×4	3×3×1
25% Sn/Ru(0001)	5 (3)	4×4	3×3×1
50% Sn/Ru(0001)	5 (3)	4×4	3×3×1
SnO/Ru(0001)	3 (2)	5×5	3×3×1

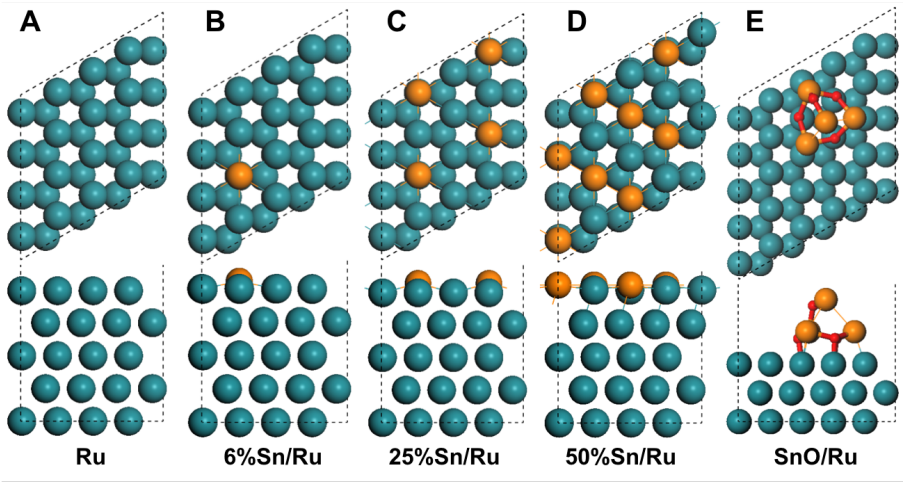

Figure S7. RuSn models used in this work:(A) Ru(0001), (B) 6% Sn/Ru(0001), (C) 25% Sn/Ru(0001), (D) 50% Sn/Ru(0001), (E) and SnO/Ru(0001).

Hydrogen coverage dependence

Hydrogen adsorption energies as a function of coverage are provided in **Figure S8**. The interpolations herein were used in plotting atomistic thermodynamics phase diagrams, which then show surface coverage on a continuous basis.

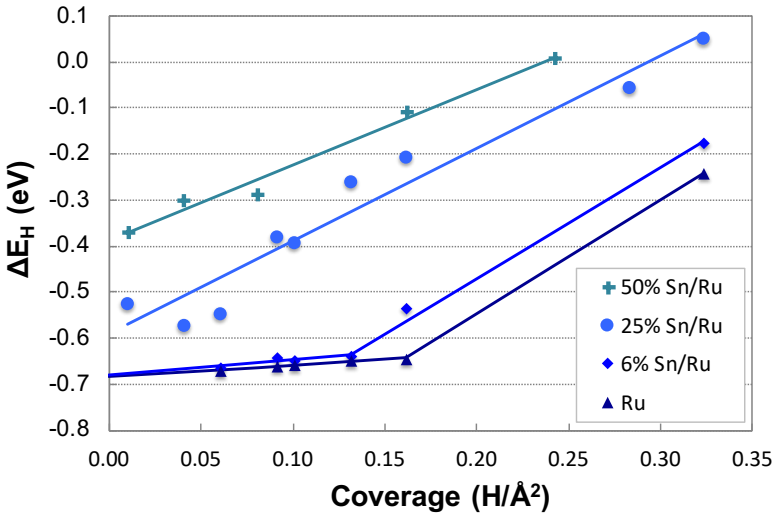

Figure S8. Average hydrogen adsorption energy as a function of coverage for four model metallic surfaces addressed in the manuscript.

Hydrogen dissociation

Hydrogen dissociation curves over Ru sites of Ru(0001), 25% Sn/Ru(0001), and 50% Sn/Ru(0001) are shown in **Figure S9**. The barrier for H_2 dissociation over SnO/Ru(0001) was found to be 99 kJ mol^{-1} using standard cNEB and dimer approach.

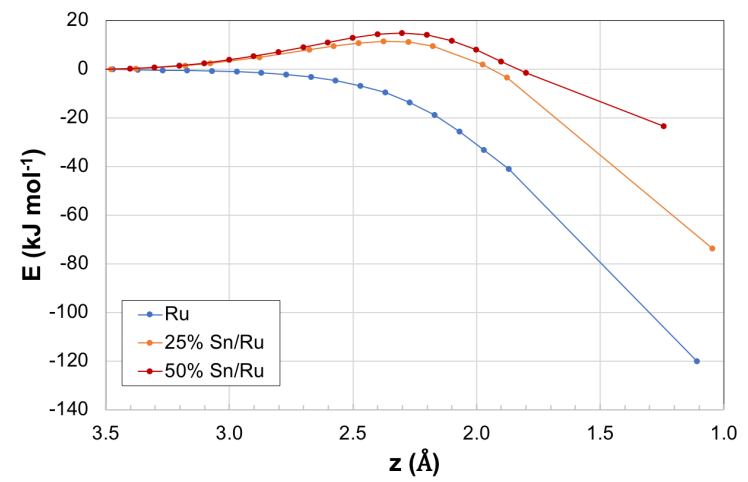

Figure S9. Hydrogen dissociation curves over Ru sites of three model surfaces. Parameter z (x-axis) refers to the vertical distance between the top slab layer and the H_2 molecule. In these simulations, surface atoms were frozen in their optimized "clean" surface geometries, while the H_2 molecule was allowed to relax in the two dimensions parallel to the surface (i.e. x and y) for each value of z. All energies are referenced to H_2 molecule placed in the vacuum between periodic slabs.

Brønsted-Evans-Polanyi (BEP) Relations

Performing DFT calculations for all possible reactions is impractical when dealing with larger molecules (C_2+) and multiple catalytic surfaces. However, reaction-specific BEP relations can alleviate this need, providing insight into the underlying reactivity trends.[17, 18] In this work, we utilize DFT results from previous works[22, 24] to build BEP relations for C-H, O-H, C-C, and C-O scission and use them in conjunction with reaction energies computed in this work. This allows us to estimate intrinsic energetic profiles for propionic acid initial cracking (and hydrogenation to propanol) over Ru(0001) and Sn/Ru(0001) surfaces.

The key criteria chosen for BEP development in this work included (i) similar surface, i.e. Ru(0001), (ii) DFT functional based on generalized gradient approximation (GGA), (iii) similarity of involved species, i.e. linear oxygenates and alkanes and (iv) higher saturation of surface intermediates. The last consideration addresses the concern that BEP relations are structure-sensitive and that higher level of dehydrogenation results in greater conformational differences and, by extension, deviations from the trend.[18, 26] Studying higher saturation levels was sufficient for this work; however, if highly dehydrogenated species are of interest, new BEP relations may need to be explored. Following our criteria (i)-(iv), we show that the resulting BEPs reveal new structure-sensitive trends and provide higher-accuracy estimates specific to Ru(0001) surfaces.

To develop BEP relations, we compiled DFT results from the work on methanol,[23, 25] ethanol,[22, 26] hexadecanol,[21] C_1-C_4 aldehydes and ketones,[27, 28] acetic acid,[29, 30] propionic acid,[24] and levulinic acid.[31] The resulting BEP relations used to estimate barriers in this work are summarized in **Table S3.** Improvement in parameter estimates was achieved by using larger data sets and by the introduction of structure specificity. Statistical confidence in some BEP relations, such as physisorbed C-C or C-OH scission, suffers from the lack of available data as demonstrated by combining the two BEPs into a single, heteroatom-heteroatom scission (C-C/C-OH physisorbed), effectively reducing the uncertainty in the associated slope and intercept while providing similar mean absolute error (MAE) estimates. Our analysis shows that C-OH scission of chemisorbed intermediates (C-OH chemisorbed) and C-OH scission of carboxylic acids (C-OH acid) have statistically different intercepts in their corresponding BEP's, which is reflected in significantly lower barriers in carboxylic acid C-OH bond cleavage. More details on each BEP relation are available below.

Table S3. Summary of BEP relations used in this work. AE is the absolute error, N is the number of points used in regression, and the ± values represent the 95% confidence interval on parameter estimates. Regression was performed based on Ru(0001) DFT results with the exception of "C-OH acid (all)", which also included metal-doped Cu surfaces.[30]

BEP	m	b (eV)	Mean AE (eV)	Max AE (eV)	N	ΔE range (eV)
C-H	0.83 ± 0.04	0.70 ± 0.12	0.11	0.37	68	(-1.00, 0.49)
C-H (SnO/Ru)	0.33 ± 0.41	1.33 ± 0.89	0.17	0.37	6	(-0.20,0.71)
O-H	0.47 ± 0.11	0.88 ± 0.17	0.12	0.33	52	(-1.13, 0.01)
O-H (SnO/Ru)	0.60 ± 0.26	0.35 ± 0.53	0.06	0.11	5	(-0.65, -0.01)
C-O	0.83 ± 0.32	1.47 ± 0.50	0.17	0.38	9	(-1.11, -0.02)
Combined C-C/C-OH physisorbed	1.13 ± 0.23	2.04 ± 0.74	0.16	0.31	7	(-0.45, 0.42)
C-C physisorbed	0.80	2.21	0.15	0.23	3	(0.12, 0.42)
C-OH physisorbed	0.74 ± 0.68	1.90 ± 2.12	0.16	0.24	4	(-0.45,0.21)
C-C chemisorbed	0.67 ± 0.08	1.16 ± 0.15	0.13	0.33	26	(-1.21, 0.95)
C-OH chemisorbed	0.86 ± 0.12	1.28 ± 0.17	0.08	0.29	16	(-1.14, 0.49)
C-OH acid	0.90 ± 0.62	0.73 ± 1.41	0.06	0.11	4	(-0.66, -0.26)
C-OH acid (all)	0.92 ± 0.09	0.67 ± 0.18	0.10	0.19	11	(-0.66, 0.92)

C-H Scission

In addition to criteria (i)-(iv) for BEP development, we excluded three outliers from the fitting set based on the maximum normal residual test with 5% significance. First, the test identified two reactions, CH3O → CH2O + H and CHOH → COH + H, from Liu et al.[23] as outliers. These reactions showed barriers 0.82 and 0.7 eV higher than the corresponding values obtained by Moura et al.[25] The other barrier excluded from the fitting set was CH2CHOH → CH2COH + H.[26] The DFT results used for regression are tabulated in **Table S4**. The BEP relation is shown in **Figure S10**. The MAE in barrier estimates for this BEP relation is 0.11 eV compared with the BEP relation developed for ethanol alone (and higher dehydrogenation levels), which gives 0.31 eV.

Table S4a. C-H scission reactions on Ru(0001) used in developing the corresponding BEP.

#	Reaction	ΔE (eV)	E_A (eV)	Source
1	CH3CH2OH --> CH3CHOH + H	0.00	0.94	
2	CH3CH2OH --> CH2CH2OH + H	0.03	0.80	
3	CH3CH2O --> CH3CHO + H	0.11	0.80	
4	CH2CH2OH --> CH2CHOH + H	-0.26	0.40	
5	CH3CH2O --> CH2CH2O + H	0.34	0.97	22
6	CH3CHOH --> CH2CHOH + H	-0.24	0.30	
7	CH3CHOH --> CH3COH + H	-0.27	0.36	
8	CH3CHO --> CH2CHO + H	-0.36	0.33	
9	CH3COH --> CH2COH + H	-0.21	0.55	
10	CH3CHO --> CH3CO + H	-0.57	0.12	
11	CH3CH2COOH --> CH3CHCOOH + H	-0.3	0.56	
12	CH3CH2COO --> CH3CHCOO + H	0.05	0.75	
13	CH3CHCOOH --> CH2CHCOOH + H	-0.51	0.52	24
14	CH3CHCOOH --> CH3CCOOH + H	-0.48	0.62	
15	CH3CHCOO --> CH3CCOO + H	0.22	0.94	
16	CH2CHCOOH --> CHCHCOOH + H	-0.35	0.27	
17	CH3CH2OH --> CH3CHOH + H	-0.03	0.72	
18	CH3CH2O --> CH3CHO + H	0.09	0.83	29
19	CH3CHOH --> CH3COH + H	-0.3	0.37	
20	CH3CHO --> CH3CO + H	-0.61	0.21	
21	CH3CH2OH --> CH3CHOH + H	-0.27	0.72	
22	CH3CH2OH --> CH2CH2OH + H	-0.01	0.52	
23	CH3CHOH --> CH3COH + H	-0.39	0.3	
24	CH2CH2OH --> CH2CHOH + H	-0.52	0.12	
25	CH3CH2O --> CH3CHO + H	-0.1	0.65	
26	CH2CH2OH --> CHCH2OH + H	-0.57	0.13	
27	CH3CH2O --> CH2CH2O + H	0.17	0.74	26
28	CH3CHO --> CH3CO + H	-0.63	0.16	
29	CH2CH2O --> CH2CHO + H	-0.61	0.26	
30	CH3COH --> CH2COH + H	-0.25	0.50	
31	CH2CHOH --> CH2CHOH + H	-0.51	0.09	
32	CHCH2OH --> CCH2OH + H	-0.62	0.34	
33	CH3CHO --> CH2CHO + H	-0.35	0.46	
34	CH2CH2O --> CHCH2O + H	-0.19	0.32	

Table S4b. C-H scission reactions on Ru(0001) used in developing the corresponding BEP, continued. (R stands for $C_{14}H_{29}$).

#	Reaction	ΔE (eV)	E_A (eV)	Source
35	RCH2CH2OH --> RCH2CHOH + H	0.13	0.85	
36	RCH2CH2OH --> RCHCH2OH + H	0.21	1.08	
37	RCH3 --> RCH2 + H	0.11	0.96	
38	RCH2CH3 --> RCH2CH2 + H	-0.12	0.91	
39	RCH2CH2O --> RCH2CHO + H	-0.14	0.36	
40	RCH2CH2O --> RCHCH2O + H	0.27	1.01	[21]
41	RCH2 --> RCH + H	-0.54	0.29	
42	RCH2CH2 --> RCH2CH + H	-0.17	0.26	
43	RCH2CHO -->RCHCHO + H	-0.43	0.50	
44	RCH2CHO --> RCH2CO + H	-0.74	0.09	
45	RCHCH2 --> RCHCH + H	-0.04	0.48	
46	RCH2CH --> RCHCH + H	-0.27	0.11	
47	CH3OH --> CH2OH + H	0.13	0.66	
48	CH3O --> CH2O + H	-0.02	0.63	[25]
49	CH2OH --> CHOH + H	-0.23	0.70	
50	CHOH --> COH + H	-1.00	0.00	
51	CH3OH --> CH2OH + H	0.11	0.97	
52	CH2OH --> CHOH + H	-0.05	0.43	[23]
53	CH2O --> CHO + H	-0.29	0.33	
54	CH3CH(OH)CH2CH2COOH --> CH3C(OH)CH2CH2COOH + H	0.05	0.81	
55	CH3CH(O)CH2CH2COOH --> CH3C(=O)CH2CH2COOH + H	-0.06	0.61	[31]
56	CH3CH(O)CH2CH2COO --> CH3C(=O)CH2CH2COO + H	-0.45	0.23	
57	CH3OH --> CH2OH + H	-0.15	0.79	
58	CH3CH2OH --> CH3CHOH + H	-0.09	0.73	
59	CH3CH2CH2OH --> CH3CH2CHOH + H	-0.07	0.70	
60	CH3CH(OH)CH3 --> CH3C(OH)CH3 + H	0.01	0.80	
61	CH3CH2CH2CH2OH --> CH3CH2CH2CHOH + H	0.07	0.80	
62	CH3CH(OH)CH2CH3 --> CH3C(OH)CH2CH3	0.10	0.85	[27]
63	CH3O --> CH2O + H	0.03	0.70	
64	CH3CH2O --> CH3CHO + H	0.15	0.80	
65	CH3CH2CH2O --> CH3CH2CHO + H	0.07	0.67	
66	CH3CH(O)CH3 --> CH3C(O)CH3 + H	0.25	0.80	
67	CH3CH2CH2CH2O --> CH3CH2CH2CHO + H	0.09	0.77	
68	CH3CH(O)CH2CH3 --> CH3C(O)CH2CH3	0.49	1.09	

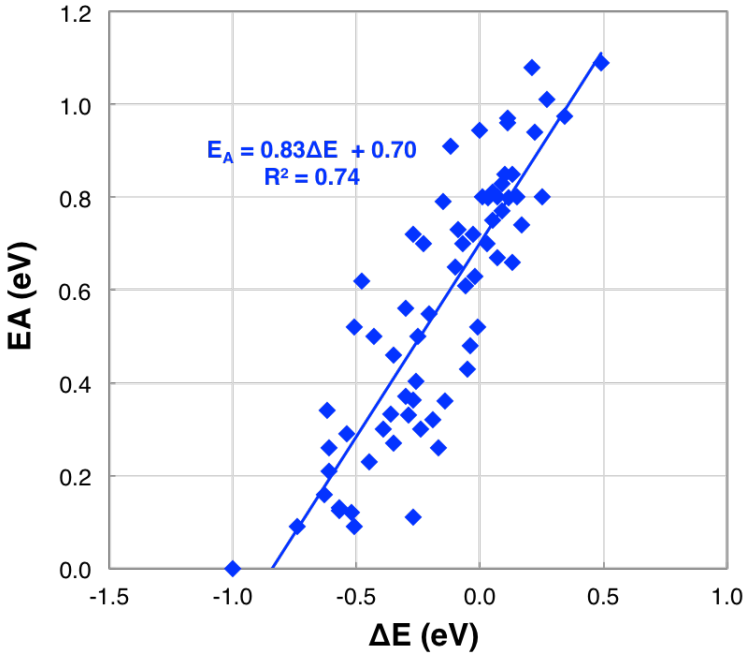

Figure S10. C-H Scission BEP for Ru(0001).

O-H Scission

The DFT results used for regression are tabulated in **Table S5**. The BEP relation is shown in **Figure S11**. The correlation here is rather weak, which is reflected in comparable MAE values for BEP relations developed here compared to those developed for ethanol-related intermediates alone[26] (0.12 eV and 0.15 eV, respectively).

Table S5. O-H scission reactions on Ru(0001) used in developing the corresponding BEP (R stands for $C_{14}H_{29}$).

#	Reaction	ΔE (eV)	EA (eV)	Source
1	CH3CH2OH --> CH3CH2O + H	-0.60	0.72	22
2	CH3CHOH --> CH3CHO + H	-0.50	0.68	
3	CH2CH2OH --> CH2CH2O + H	-0.29	0.70	
4	CH3COH --> CH3CO + H	-0.79	0.45	
5	CH3CH2COOH --> CH3CH2COO + H	-1.02	0.21	24
6	H2O --> OH + H	-0.61	0.61	
7	CH3CHCOOH --> CH3CHCOO + H	-0.68	0.39	
8	CH3CCOOH --> CH3CCOO + H	0.01	1.17	
9	CH3COOH --> CH3COO + H	-0.96	0.36	29
10	CH3CH2OH --> CH3CH2O + H	-0.61	0.71	
11	H2O --> OH + H	-0.41	0.81	
12	CH3CHOH --> CH3CHO + H	-0.49	0.72	
13	OH --> O + H	-0.82	0.74	
14	CH3COH --> CH3CO + H	-0.8	0.45	
15	CH3CH2OH --> CH3CH2O + H	-0.67	0.65	26
16	CH3CHOH --> CH3CHO + H	-0.5	0.72	
17	CH2CH2OH --> CH2CH2O + H	-0.5	0.38	
18	CH3COH --> CH3CO + H	-0.74	0.53	
19	CH2CHOH --> CH2CHO + H	-0.59	0.43	
20	CHCH2OH --> CHCH2O + H	-0.12	0.67	
21	RCH2CH2OH --> RCH2CH2O + H	-0.3	0.72	21
22	CH3OH --> CH3O + H	-0.38	0.49	25
23	CH2OH --> CH2O + H	-0.45	0.43	
24	CH3OH --> CH3O + H	-0.24	0.74	23
25	CH2OH --> CH2O + H	-0.35	0.67	
26	OH --> O + H	-0.62	0.78	
27	CHOH --> CHO + H	-0.4	0.65	
28	CH3CH(OH)CH2CH2C(OH)OH --> CH3CH(OH)CH2CH2COOH + H	-0.55	0.47	31
29	H2O --> OH + H	-0.58	0.58	
30	CH3CHCH2CH2COOH --> CH3CHCH2CH2COO + H	-0.98	0.34	
31	OH --> O + H	-0.84	0.65	
32	CH3C(=O)CH2CH2COOH --> CH3C(=O)CH2CH2COO + H	-1.13	0.06	
33	CH3C(OH)CH2CH2C(OH)OH --> CH3C(OH)CH2CH2COOH + H	-1.06	0.35	
34	CH3CH(OH)CH2CH2COH --> CH3CH(OH)CH2CH2CO + H	-0.83	0.71	
35	CH3CH(OH)CH2CH2COOH --> CH3CH(O)CH2CH2COOH + H	-0.76	0.53	
36	CH3C(OH)CH2CH2COOH --> CH3C(=O)CH2CH2COOH + H	-0.88	0.48	
37	CH3CH(OH)CH2CH2C(OH)OH --> CH3CH(O)CH2CH2C(OH)OH + H	-0.25	0.64	
38	CH3CH(OH)CH2CH2COH --> CH3CH(O)CH2CH2COH + H	-0.44	0.59	
39	CH3OH --> CH3O + H	-0.55	0.74	27
40	CH3CH2OH --> CH3CH2O + H	-0.66	0.66	
41	CH3CH2CH2OH --> CH3CH2CH2O + H	-0.63	0.68	
42	CH3CH2CH2CH2OH --> CH3CH2CH2CH2O + H	-0.58	0.72	
43	CH2OH --> CH2O + H	-0.38	0.55	
44	CH3CHOH --> CH3CHO + H	-0.42	0.72	
45	CH3CH2CHOH --> CH3CH2CHO + H	-0.49	0.77	
46	CH3CH2CH2CHOH --> CH3CH2CH2CHO + H	-0.53	0.78	
47	CH3CH(OH)CH3 --> CH3CH(O)CH3 + H	-0.61	0.69	
48	CH3CH(OH)CH2CH3 --> CH3CH(O)CH2CH3	-0.53	0.76	
49	CH3C(OH)CH3 --> CH3C(O)CH3 + H	-0.51	0.81	
50	CH3C(OH)CH2CH3 --> CH3C(O)CH2CH3	-0.23	0.44	
51	CH3CH(OH)CH3 --> CH3CH(O)CH3 + H	-0.58	0.79	28
52	CH3C(OH)CH3 --> CH3C(O)CH3 + H	-0.51	0.72	

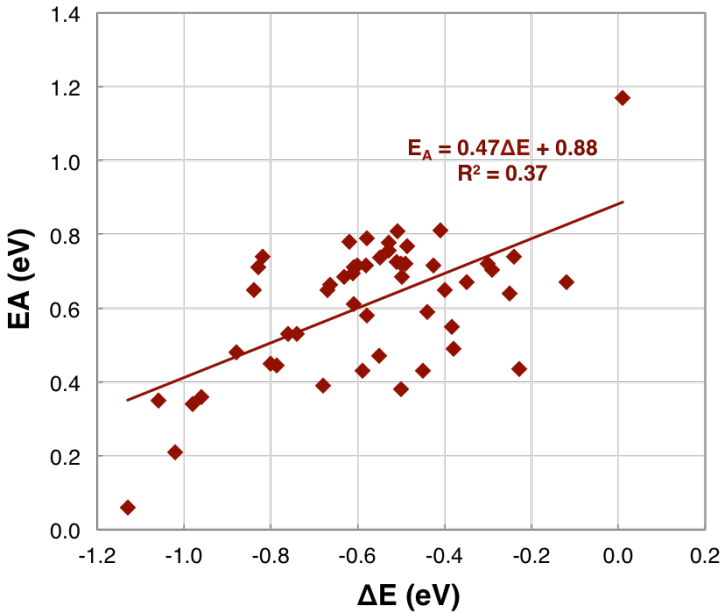

Figure S11. O-H Scission BEP for Ru(0001).

C-C Scission

In addition to criteria (i)-(iv) for BEP development, we excluded one outlier from the fitting set based on the maximum normal residual test with 5% significance. The barrier for reaction CH3COH → CH3 + COH was found to be 1.35 eV[26] compared to 0.95 eV computed by Chiu et al.[22] while reaction energies were the same at -0.58 eV. Furthermore, we find that the saturation level of carbon atoms involved in C-C bond cleavage significantly affects the intercept of the BEP relation, effectively introducing structure dependence. The DFT results used for regression are tabulated in **Table S6**. The BEP relations is shown in **Figure S12**. The resulting BEP correlations developed here result in MAE of 0.13 eV, substantially lower than a single, structure-independent BEP relation developed for ethanol decomposition intermediates alone (0.25 eV).[26]

Table S6. C-C scission reactions on Ru(0001) used in developing the corresponding BEP (R stands for $C_{14}H_{29}$).

#	Reaction	ΔE (eV)	EA (eV)	Source
1	CH3CH2OH --> CH3 + CH2OH	0.25	2.64	22
2	CH3CH2O --> CH3 + CH2O	0.42	2.45	
3	CH3CH2O --> CH3 + CH2O	0.12	2.18	26
4	CH2CH2OH --> CH2 + CH2OH	0.07	1.32	22
5	CH3CHO --> CH3 + CHO	-0.03	1.07	
6	CH2CH2O --> CH2 + CH2O	-0.06	1.05	
7	CH3COH --> CH3 + COH	-0.58	0.95	
8	CH2COH --> CH2 + COH	-0.52	0.95	
9	CHCHO --> CH + CHO	-0.15	1.08	
10	CH3CHCOOH --> CH3CH + COOH	-0.21	0.89	24
11	CH3CH2COO --> CH3CH2 + CO2	0.95	1.71	
12	CH2CHCOOH --> CH2CH + COOH	-0.09	0.94	
13	CH3CHCOO --> CH3CH + CO2	0.22	1.18	
14	CH3CH2CO --> CH3CH2 + CO	-0.41	0.84	
15	CH3CCOO --> CH3C + CO2	-0.69	0.44	
16	CH3CHCO --> CH3CH + CO	-0.66	0.85	
17	CH2CHCO --> CH2CH + CO	-0.61	0.98	
18	CH3CCO --> CH3C + CO	-0.98	0.36	
19	CH2CH2OH --> CH2 + CH2OH	-0.3	1.11	26
20	CH3CHOH --> CH3 + CHOH	-0.15	1.39	
21	CH3CHO --> CH3 + CHO	-0.23	1.08	
22	CHCH2OH --> CH + CH2OH	-0.06	1.30	
23	CHCH2O --> CH + CH2O	-0.44	0.80	
24	CH3CO --> CH3 + CO	-0.59	0.79	
25	CH2COH --> CH2 + COH	-0.58	0.65	
26	CH2CO --> CH2 + CO	-1.21	0.41	
27	RCHCO --> RCH + CO	-0.82	0.54	21
28	CH2CO --> CH2 + CO	-0.47	0.74	32
29	CHCO --> CH + CO	-0.65	0.49	

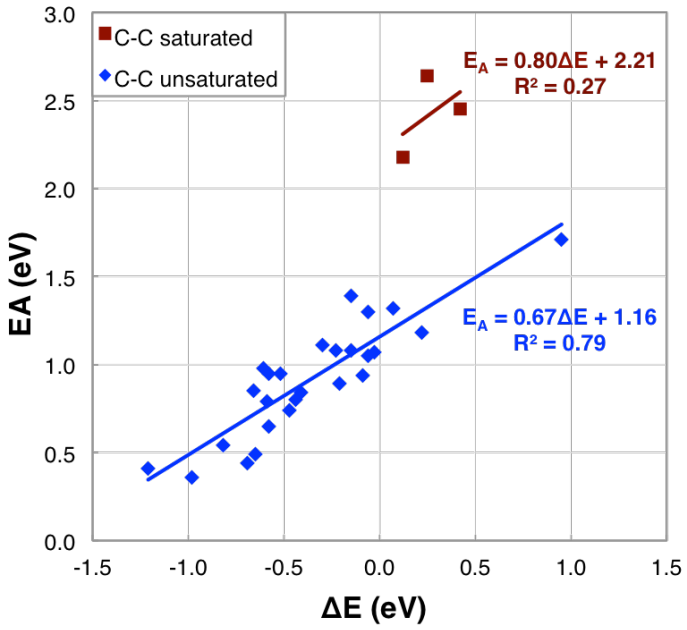

Figure S12. C-C Scission BEP for Ru(0001). The two relations represent the saturation level of C atoms involved in C-C scission: fully saturated (red) and partially dehydrogenated (blue).

C-OH Scission

Similar to C-C bond cleavage reactions, we grouped the C-OH scission reactions into subgroups based on the saturated level of the initial state. The main two groups are fully saturated (physisorbed) and bound (chemisorbed) intermediates. We also found that the alcohol C-OH scission appears to be inherently different from carboxylic acid C-OH scission, showing particularly lower barriers, resulting in a different BEP correlation. The DFT results used for regression are tabulated in **Table S7**. The BEP relations are shown in **Figure S13**. The resulting BEP correlations result in MAE of 0.09 eV, substantially improved over ethanol-based BEP MAE of 0.49 eV.[26]

Table S7. C-OH scission reactions on Ru(0001) used in developing the corresponding BEP (R stands for $C_{14}H_{29}$) and acetic acid C-OH scission reactions for M-doped Cu(111) surfaces.

#	Reaction	ΔE (eV)	EA (eV)	Source
1	CH3CH2OH --> CH3CH2 + OH	-0.33	1.73	22
2	RCH2CH2OH --> RCH2CH2 + OH	-0.24	1.97	21
3	CH3OH --> CH3 + OH	-0.45	1.35	25
4	CH3OH --> CH3 + OH	0.21	1.97	23
5	C5H10O3 --> C5H9O2 + OH	-0.34	0.99	31
6	C5H8O3 --> C5H7O2 + OH	-0.61	0.71	
7	C5H9O3 --> C5H8O2 + OH	-0.61	0.84	
8	C5H10O3 --> C5H9O2 + OH	-0.56	0.75	
9	CH3CHCOOH --> CH3CHCO + OH	-0.44	0.61	24
10	CH2CHCOOH --> CH2CHCO + OH	-0.37	0.99	
11	COOH --> CO + OH	-0.89	0.34	
12	CH3CHOH --> CH3CH + OH	-0.74	0.57	22
13	CH2CH2OH --> CH2CH2 + OH	-0.69	0.83	
14	CH3COH --> CH3C + OH	-1.14	0.34	
15	CH2CHOH --> CH2CH + OH	-0.70	0.73	
16	CH2COH --> CH2C + OH	-0.88	0.68	
17	CHCHOH --> CHCH + OH	-0.80	0.65	
18	CH2OH --> CH2 + OH	-0.30	1.06	23
19	CHOH --> CH + OH	-1.07	0.29	
20	COH --> C + OH	0.49	1.73	
21	CH3CH2COOH --> CH3CH2CO + OH	-0.36	0.49	24
22	CH3COOH --> CH3CO + OH	-0.26	0.52	29
23	C5H10O3 --> C5H9O2 + OH	-0.66	0.15	31
24	C5H11O3 --> C5H10O2 + OH	-0.37	0.29	
25	CH3COOH --> CH3CO + OH: CoCu	-0.38	0.14	30
26	CH3COOH --> CH3CO + OH: NiCu	0.08	0.55	
27	CH3COOH --> CH3CO + OH: RuCu	-0.09	0.66	
28	CH3COOH --> CH3CO + OH: RhCu	0.24	0.74	
29	CH3COOH --> CH3CO + OH: PdCu	0.74	1.47	
30	CH3COOH --> CH3CO + OH: PtCu	0.59	1.23	
31	CH3COOH --> CH3CO + OH: Cu	0.92	1.53	

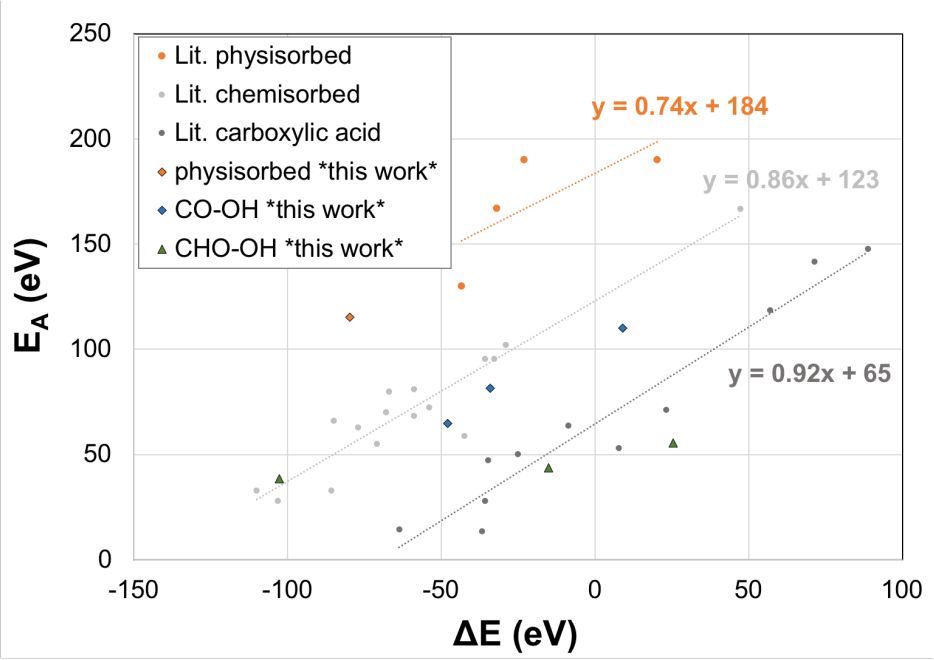

Figure S13. C-OH Scission BEP relations for Ru(0001). The three sets are grouped based on initial state structure: fully saturated/physisorbed (top set), chemisorbed/bound species (middle), and carboxylic acids (bottom). The carboxylic acids set also includes Cu(111) doped with various metals for acetic acid dehydroxylation.[30] CO-OH refers to direct carboxylic acid dehydroxylation, while CHO-OH refers to once-hydrogenated carboxylic acid dehydroxylation.

C-O Scission

The literature is less extensive for C-O bond scission. The DFT results used for regression are tabulated in **Table S8**. The BEP relation is shown in **Figure S14**. The resulting correlation shows MAE of 0.17 eV, comparable to ethanol-based BEP MAE of 0.23 eV for the same set.[26] We did not attempt to re-group this set due to the lack of literature values.

Table S8. C-O scission reactions on Ru(0001) used in developing the corresponding BEP (R stands for $C_{14}H_{29}$).

#	Reaction	ΔE (eV)	EA (eV)	Source
1	CH3CH2O --> CH3CH2 + O	-0.44	1.41	
2	CH3CHO --> CH3CH + O	-0.94	0.83	[22]
3	CH2CH2O --> CH2CH2 + O	-1.11	0.45	
4	CH3CH2O --> CH3CH2 + O	-0.14	1.34	
5	CH2CH2O --> CH2CH2 + O	-0.88	0.58	[26]
6	CH3CHO --> CH3CH + O	-0.66	0.84	
7	RCH2CH2O --> RCH2CH2 + O	-0.14	1.66	[21]
8	CH2O --> CH2 + O	-0.35	1.14	
9	CH3COO --> CH3CO + O	-0.02	1.07	[29]

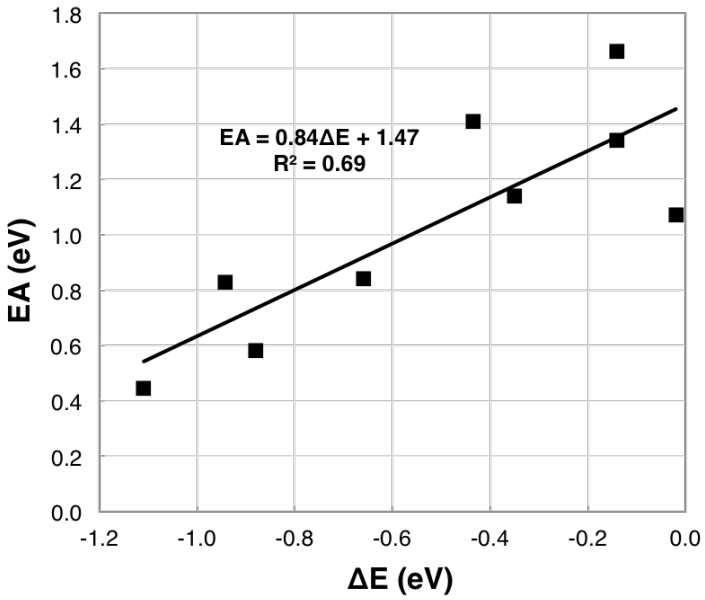

Figure S14. C-O Scission BEP relation on Ru(0001).

On BEP Limitations

Since BEP relations represent the regression of DFT-obtained results, they are inherently limited by the reported calculations. For instance, to the best of our knowledge, there are currently no available DFT results studying the effect of Sn incorporation into Ru surface on hydrocarbon or oxygenate kinetics. Therefore, we are limited by Ru(0001) studies of related chemistry. Nonetheless, recent work on Sn/Pt(111) with similar modeling of Sn incorporation clearly show that Sn incorporation does not change the underlying BEP relations, at least considering C-H scission.

C-H Scission over Pt(111) vs. Sn/Pt(111)

In estimating barriers along reactions leading to cracking, we assumed that BEP relations developed for R(0001) will hold true for Sn/Ru(0001) as well. The universality of BEP relations has been demonstrated for metallic close-packed surfaces in the past.[19, 20] To further exemplify this effect specific to Sn-substituted bimetallic surfaces, we refer to Sn/Pt literature,[33, 34] where C-H scission of ethane and propane were investigated over Pt(111), 25% Sn/Pt(111), and 50% Sn/Pt(111), similarly to our current work. We compiled these results in **Table S9** and performed linear regression on the Pt(111) set only to obtain a BEP relation as shown in **Figure S15**. The Pt(111) BEP relation predicts Sn/Pt(111) barriers with a mean absolute error (MAE) of 0.14 eV, which is comparable to the results for C-H scission on Ru(0001) alone[26] (0.17 eV) and other transition metals[19] (0.28 eV). On the basis of Sn-modified metallic surfaces behaving similarly to the parent metal, we apply the Ru(0001) BEP relations to both Ru(0001) and Sn/Ru(0001) surfaces.

Table S9. C-H scission of propane intermediates over Pt(111)[33] and ethane intermediates over Pt(111) and Sn/Pt(111)[34] model surfaces used in **Figure S15**.

#	Surface	Reaction	ΔE (eV)	EA (eV)
1	Pt(111)	CH3CH2CH3 --> CH3CH2CH2 + H	-0.07	0.69
2	Pt(111)	CH3CH2CH3 --> CH3CHCH3 + H	-0.06	0.70
3	Pt(111)	CH3CH2CH2 --> CH3CHCH2 + H	-0.23	0.70
4	Pt(111)	CH3CHCH3 --> CH3CHCH2 + H	-0.24	0.68
5	Pt(111)	CH3CHCH2 --> CH3CHCH + H	0.06	0.76
6	Pt(111)	CH3CHCH2 --> CH3CCH2 + H	-0.01	0.77
7	Pt(111)	CH3CH3 --> CH3CH2 + H	0.02	0.91
8	Pt(111)	CH3CH2 --> CH3CH + H	0.11	0.91
9	Pt(111)	CH3CH2 --> CH2CH2 + H	-0.16	0.89
10	Pt(111)	CH3CH --> CH3C + H	-0.74	0.24
11	Pt(111)	CH3CH --> CH2CH + H	-0.14	0.82
12	Pt(111)	CH3C --> CH2C + H	0.41	1.42
13	Pt(111)	CH2CH2 --> CH2CH + H	0.13	0.90
14	Pt(111)	CH2CH --> CH2C + H	-0.19	0.68
15	Pt(111)	CH2CH --> CHCH + H	0.00	1.04
16	Pt(111)	CH2C --> CHC + H	1.10	1.67
17	Pt(111)	CHCH --> CHC + H	0.91	1.68
18	Pt(111)	CCH --> CC + H	0.98	1.69
19	25%Sn/Pt(111)	CH3CH3 --> CH3CH2 + H	0.28	1.19
20	25%Sn/Pt(111)	CH3CH2 --> CH3CH + H	0.27	1.04
21	25%Sn/Pt(111)	CH3CH2 --> CH2CH2 + H	0.01	1.07
22	25%Sn/Pt(111)	CH3CH --> CH3C + H	-0.36	0.49
23	25%Sn/Pt(111)	CH3CH --> CH2CH + H	0.00	0.94
24	25%Sn/Pt(111)	CH3C --> CH2C + H	0.34	1.33
25	25%Sn/Pt(111)	CH2CH2 --> CH2CH + H	0.26	1.01
26	25%Sn/Pt(111)	CH2CH --> CH2C + H	-0.01	0.82
27	25%Sn/Pt(111)	CH2CH --> CHCH + H	0.16	1.12
28	25%Sn/Pt(111)	CH2C --> CHC + H	1.13	2.00
29	25%Sn/Pt(111)	CHCH --> CHC + H	0.95	1.79
30	25%Sn/Pt(111)	CCH --> CC + H	1.12	1.88
31	50%Sn/Pt(111)	CH3CH3 --> CH3CH2 + H	0.71	1.58
32	50%Sn/Pt(111)	CH3CH2 --> CH3CH + H	0.69	1.28
33	50%Sn/Pt(111)	CH3CH2 --> CH2CH2 + H	0.36	1.28
34	50%Sn/Pt(111)	CH3CH --> CH3C + H	0.63	1.53
35	50%Sn/Pt(111)	CH3CH --> CH2CH + H	0.52	1.23
36	50%Sn/Pt(111)	CH3C --> CH2C + H	0.74	1.77
37	50%Sn/Pt(111)	CH2CH2 --> CH2CH + H	0.85	1.48
38	50%Sn/Pt(111)	CH2CH --> CH2C + H	0.52	1.23
39	50%Sn/Pt(111)	CH2CH --> CHCH + H	0.42	1.35
40	50%Sn/Pt(111)	CH2C --> CHC + H	0.96	1.47
41	50%Sn/Pt(111)	CHCH --> CHC + H	1.07	1.96
42	50%Sn/Pt(111)	CCH --> CC + H	0.33	1.56

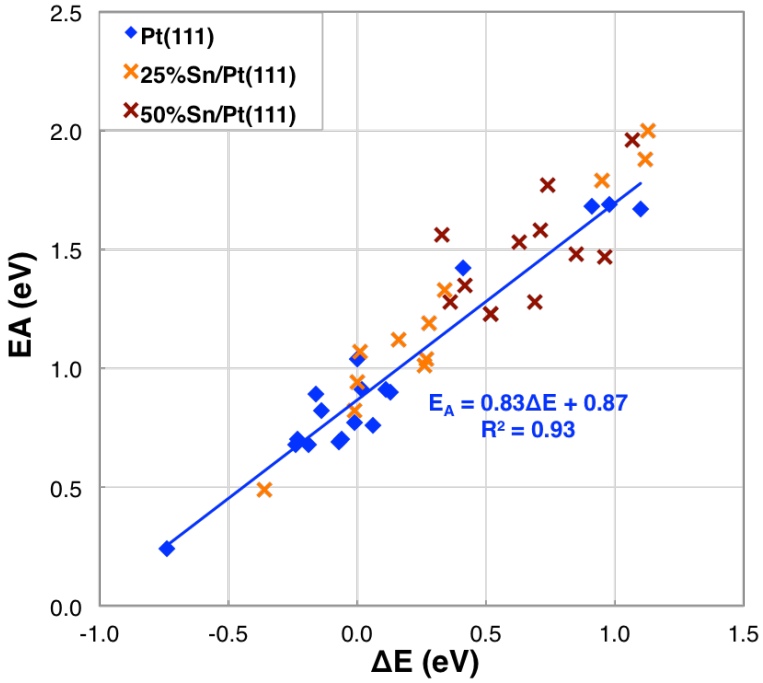

Figure S15. C-H scission BEP relation for Pt(111), 25%Sn/Pt(111) and 50%Sn/Pt(111) surfaces based on literature DFT.[33, 34] Linear regression was performed for the Pt(111) set only.

Reaction Mechanism

In this section, we report reaction energetics associated with selective and non-selective paths over Ru, Sn/Ru, and SnO/Ru catalytic functionalities. For the main reaction of propionic acid to propanol, we located all transition states with DFT. For side reactions, including over-hydrogenation, decarbonylation and decarboxylation, we computed ground state energies of the intermediates and estimated the barriers using the BEP relations (**Tables S3-9** and **Figures S9-14**). For some key side reaction steps, the BEP estimates were then refined using DFT transition state search. We then presented Gibbs free energy (T=160°C, P_{H2}=100 bar) diagrams comparing the minimum-barrier paths for each catalytic functionality. Gibbs free energies were estimated within the harmonic oscillator assumption, with the lowest frequencies (below 100 cm^{-1}) replaced with 100 cm^{-1}.

Propionic Acid Hydrogenation to Propanol

The main three reaction paths considered for propionic acid selective hydrogenation are shown in **Figure S16**.

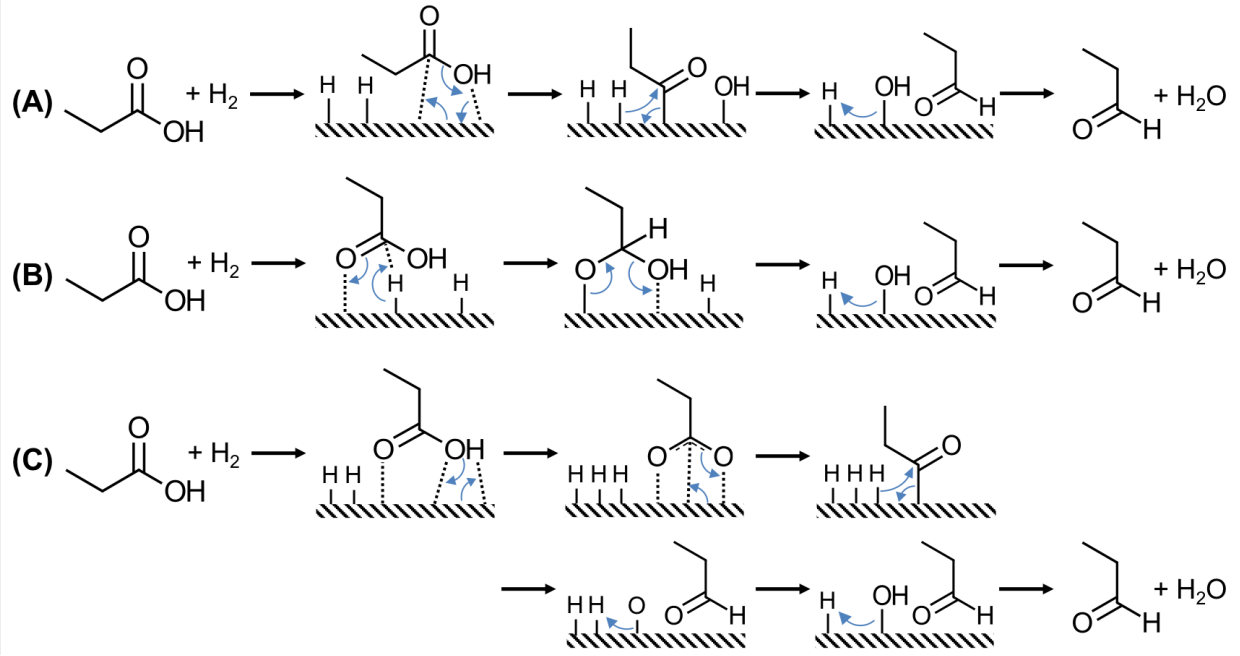

Figure S16. Reaction paths considered for propionic acid hydrogenation to propanal: (A) direct C-OH scission to propionyl followed by C-H formation, (B) C-H formation to propan-1-ol-1-olate followed by C-OH scission, and (C) O-H scission to propionate followed by C-O scission to propionyl and C-H formation.

Hydrogenation was found to proceed via two steps: (1) deoxygenation of propionic acid to propionaldehyde and (2) hydrogenation of propionaldehyde to propanol. The Gibbs free energy diagrams are presented in **Figure S17** and **Figure S18**. The Gibbs free energy diagrams for the conversion to propane over and initial reactions along the decarbonylation and decarboxylation are presented in **Figure S19** and **Figure S20**. The combined (all catalytic functionalities) Gibbs free energy diagrams for the minimum-energy paths are presented in **Figure S21** and **Figure S22**, respectively.

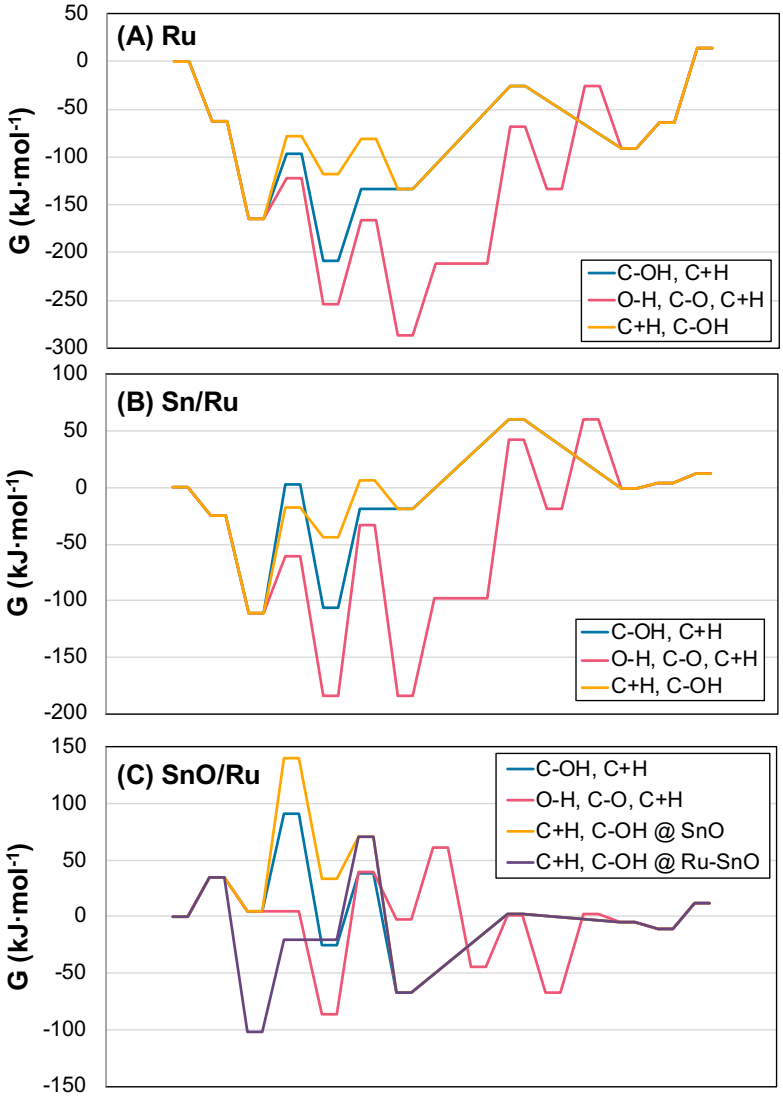

Figure S17. Gibbs free energy diagrams for propionic acid hydrogenation to propanal over (A) Ru(0001), (B) 25% Sn/Ru(0001), and (C) SnO/Ru(0001). G was computed at T=160°C, P_{H2} = 100 bar. The paths shown here correspond to those shown in **Figure S16.**

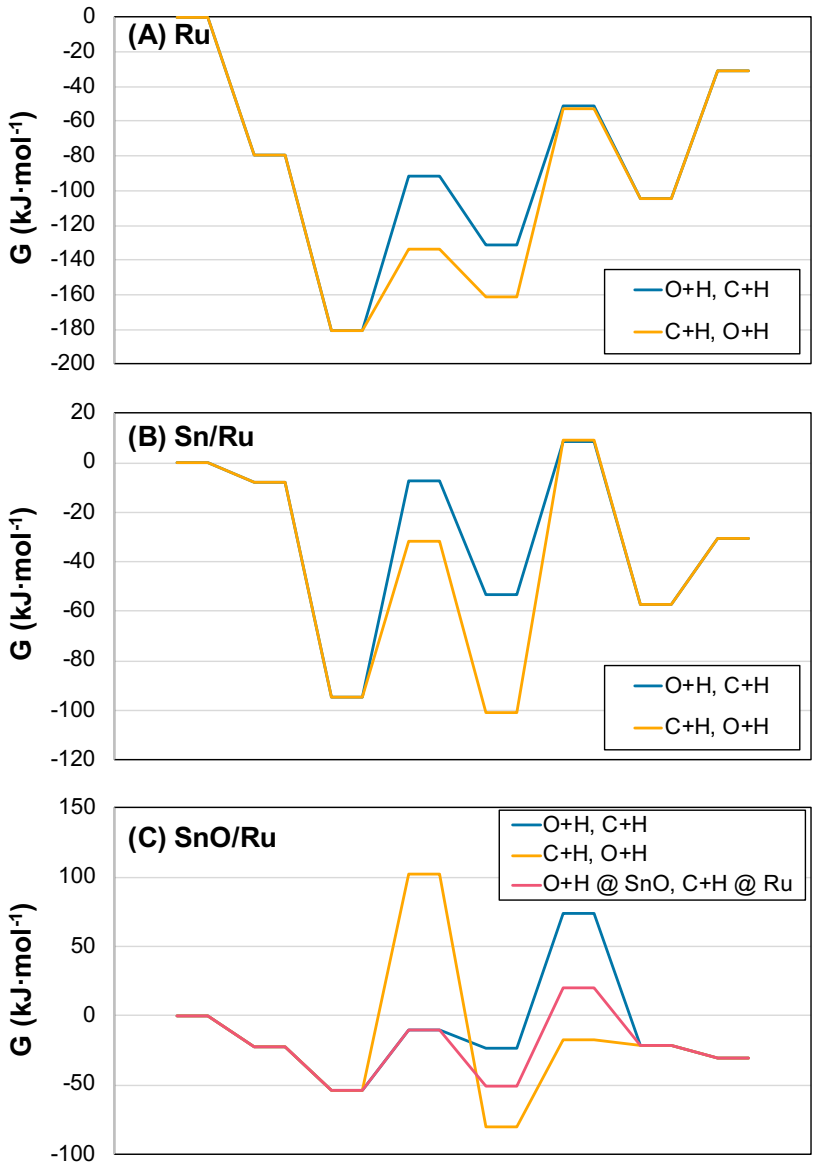

Figure S18. Gibbs free energy diagrams for propanal hydrogenation to 1-propanol over (A) Ru(0001), (B) 25% Sn/Ru(0001), and (C) SnO/Ru(0001). G was computed at T=160°C, P_{H2} = 100 bar.

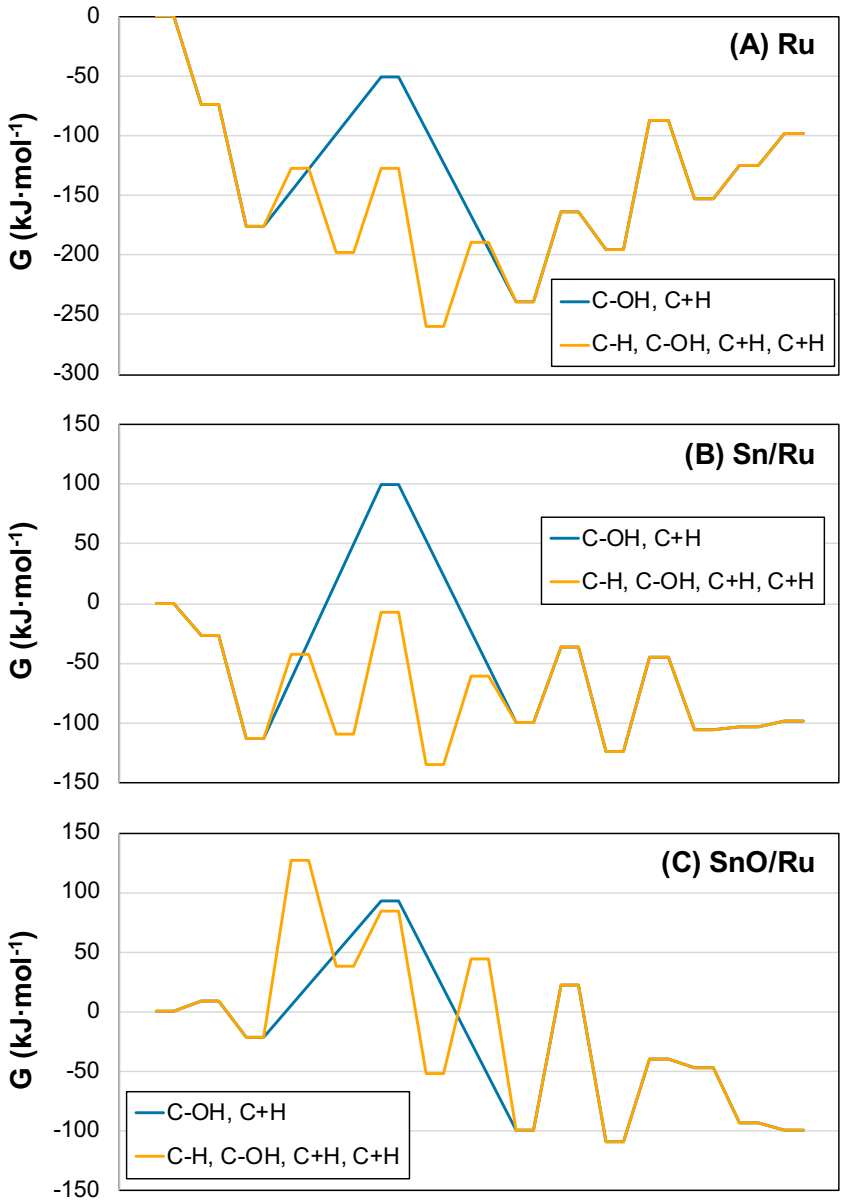

Figure S19. Gibbs free energy diagrams for 1-propanol conversion to propane over (A) Ru(0001), (B) 25% Sn/Ru(0001), and (C) SnO/Ru(0001). G was computed at T=160°C, P_{H2} = 100 bar.

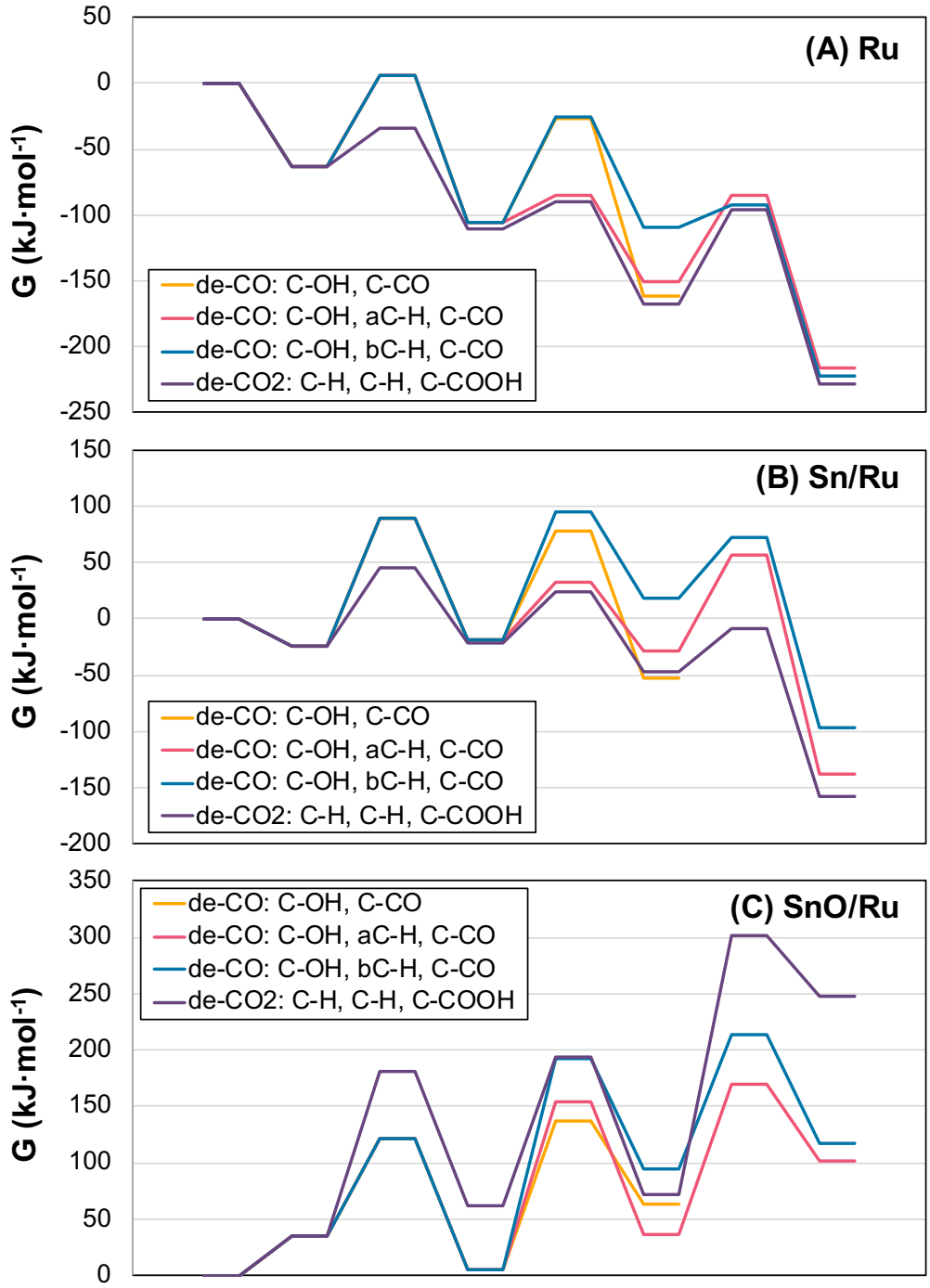

Figure S20. Gibbs free energy diagrams for initial reactions along decarbonylation and decarboxylation leading to C-C scission over (A) Ru(0001), (B) 25% Sn/Ru(0001), and (C) SnO/Ru(0001). G was computed at T=160°C, P_{H2} = 100 bar.

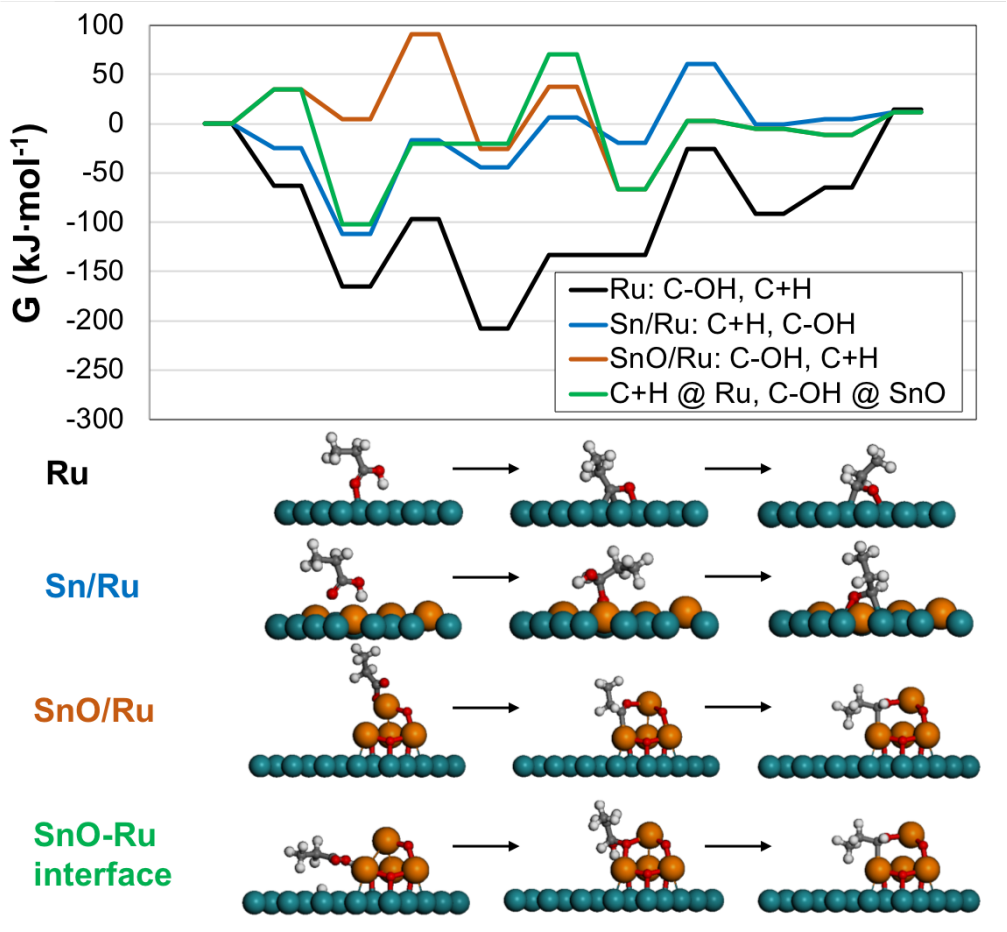

Figure S21. Propionic acid hydrogenation to propanal minimum-barrier paths on each of the catalytic functionalities considered in this work. For each functionality, the first two barriers correspond to C-H formation and C-OH scission and the last barrier is the water formation step. For clarity, the path at SnO-Ru interface proceeds via hydrogenation at the interface, followed by dehydroxylation at the SnO cluster.

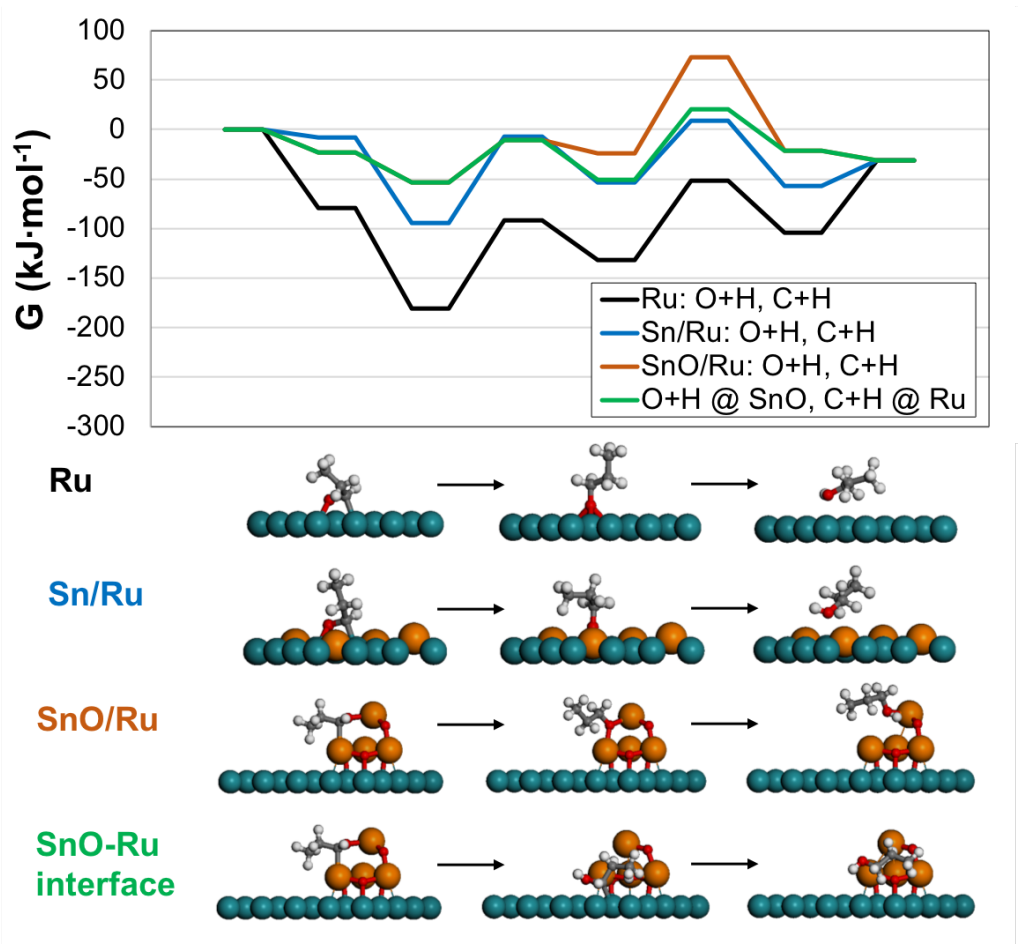

Figure S22. Propionaldehyde hydrogenation to propanol on each of the catalytic functionalities considered in this work. The path at SnO-Ru interface takes advantage of lower-barrier O-H formation at the SnO functionality together with lower-barrier C-H formation at the Ru surface.

Propanol over-hydrogenation

The paths for propanol over-hydrogenation to propane over Ru and Sn/Ru were found to necessarily proceed through C-H scission first (as has been shown for ethanol in the past). Due to the high-intercept C-H scission BEP relation, C-H scission is energetically inaccessible over SnO/Ru, making direct dehydroxylation the preferred path over SnO/Ru. The Gibbs free energy diagrams are presented in **Figure S23**.

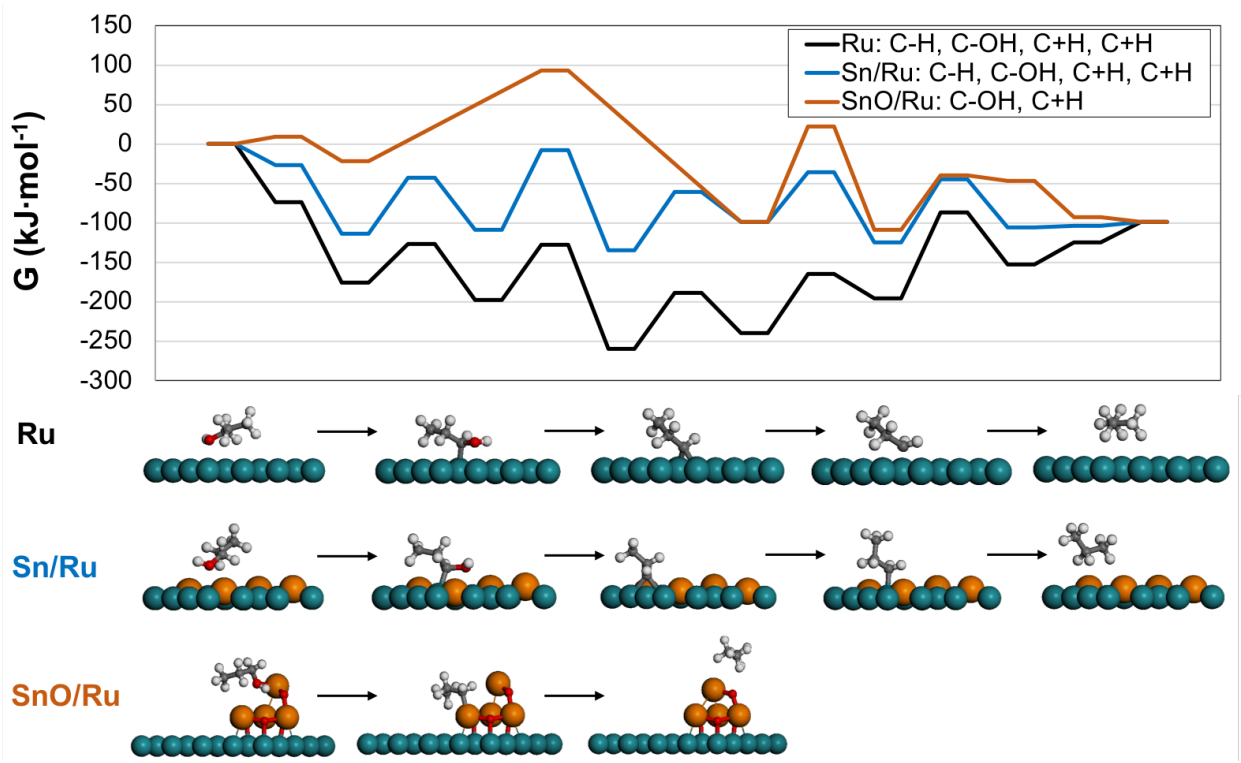

Figure S23. Over-hydrogenation of propanol to propane on each of the model surfaces considered in this work.

Cracking Paths

We considered multiple cracking pathways. For initial screening, we computed ground state energies of 31 adsorbates on Ru and Sn/Ru model surfaces, each, and used the above BEP relations to estimate the highest barriers along each considered cracking path. Zero-point energies (ZPE) were not considered in screening for the lowest-barrier paths. The results of this screening are reported in **Table S10**. While multiple paths may lead to cracking, only the minimum-barrier decarboxylation (CH3CH2COOH → CH3CHCOOH → CH3CCOOH → CH3C + COOH) and decarbonylation (CH3CH2COOH → CH3CH2CO → CH3CHCO → CH3CH + CO) paths were chosen for the overall **Scheme 1** (main text). The highlighted paths were chosen for further analysis and comparison with SnO/Ru model surface. On SnO/Ru, the minimum-barrier decarbonylation path was found to be CH3CH2COOH → CH3CH2CO → CH3CH2 + CO, which is reflected in the results below. Free energy diagrams for decarbonylation are presented in **Figure S24** and ones for decarboxylation are shown in **Figure S25**.

Table S10. Maximum barriers (kJ mol^{-1}) along various cracking paths based on BEP scaling relations. Highlighted paths were found to be lowest-barrier.

#	Path	Ru	Sn/Ru
Decarboxylation			
1	CH3CH2COOH --> CH3CH2 + COOH	105	146
2	CH3CH2COOH --> CH3CH2CHOOH --> CH3CH2 + CHOOH	135	130
3	CH3CH2COOH --> CH3CH2CHOOH --> CH3CH2CHOO --> CH3CH2 + CHOO	80	103
4	CH3CH2COOH --> CH3CH2COO --> CH3CH2 + CO2	156	167
5	CH3CH2COOH --> CH3CHCOOH --> CH3CH + COOH	108	91
6	CH3CH2COOH --> CH2CH2COOH --> CH2CH2 + COOH	76	102
7	CH3CH2COOH --> CH3CH2COO --> CH3CHCOO --> CH3CH + CO2	139	99
8	CH3CH2COOH --> CH3CH2COO --> CH2CH2COO --> CH2CH2 + CO2	108	141
9	CH3CH2COOH --> CH3CHCOOH --> CH3CHCOO --> CH3CH + CO2	139	99
10	CH3CH2COOH --> CH3CHCOOH --> CH3CCOOH --> CH3C + COOH	79	80
11	CH3CH2COOH --> CH3CHCOOH --> CH2CHCOOH --> CH2CH + COOH	154	136
12	CH3CH2COOH --> CH2CH2COOH --> CH2CHCOOH --> CH2CH + COOH	154	136
13	CH3CH2COOH --> CH2CH2COOH --> CH2CH2COO --> CH2CH2 + CO2	108	102
14	CH3CH2COOH --> CH2CH2COOH --> CHCH2COOH --> CHCH2 + COOH	131	102
Decarbonylation			
15	CH3CH2COOH --> CH3CH2CO --> CH3CH2 + CO	86	101
16	CH3CH2COOH --> CH3CH2CO --> CH3CH2CHO --> CH3CH2 + CHO	111	125
17	CH3CH2COOH --> CH3CH2CO --> CH3CH2CHO --> CH3CHCHO --> CH3CH + CHO	127	115
18	CH3CH2COOH --> CH3CH2CO --> CH3CH2CHO --> CH2CH2CHO --> CH2CH2 + CHO	86	95
19	CH3CH2COOH --> CH3CH2CO --> CH3CHCO --> CH3CH + CO	77	73
20	CH3CH2COOH --> CH3CH2CO --> CH2CH2CO --> CH2CH2 + CO	79	114

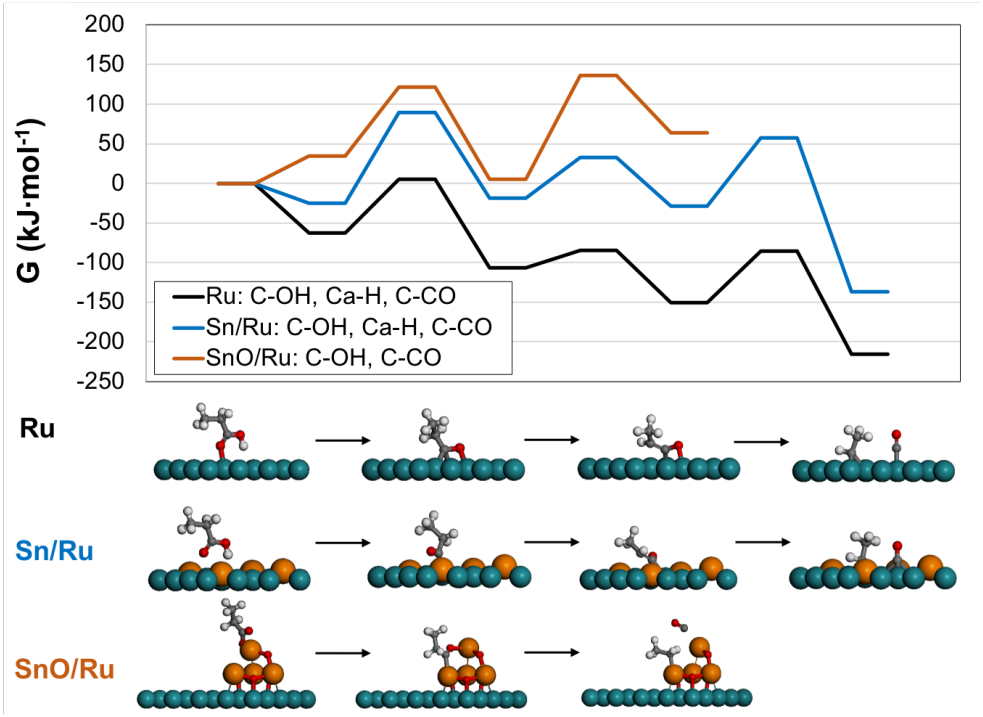

Figure S24. Lowest-barrier paths leading to decarbonylation. Only initial reaction steps were considered to highlight key differences in catalytic functionalities.

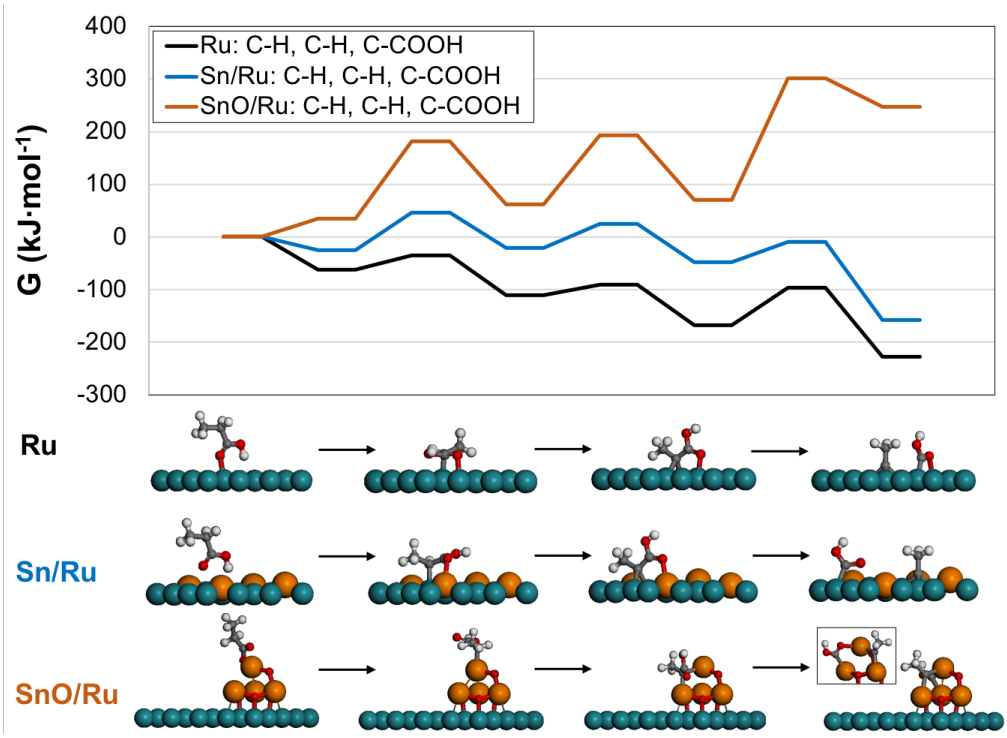

Figure S25. Lowest-barrier paths leading to decarboxylation. Only initial reaction steps were considered to highlight key differences in catalytic functionalities.

Model Comparison

We compared DFT models on the basis of highest barrier along the considered catalytic cycles or initial reactions along the path leading to decarbonylation and decarboxylation. The resulting maximum barriers are presented in **Figure S26**.

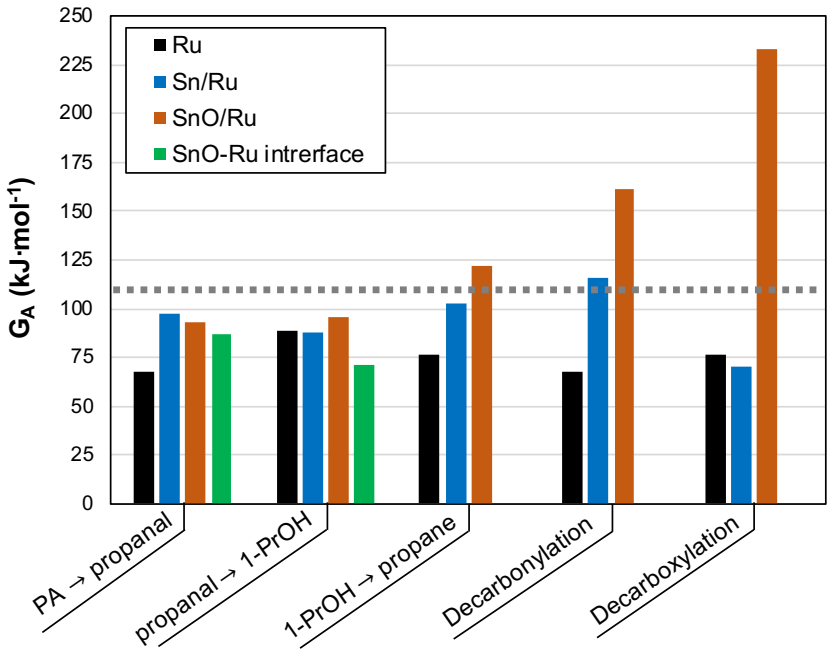

Figure S26. Maximum barriers along the lowest-barrier paths for each overall reaction considered in this work, adjusted for T=160 °C and P_{H2} = 100 bar to mimic experimental setup. The dotted line represents a threshold for barriers likely accessible at these conditions.

Reaction energetics

The computed energetics involved in the paths shown in the main report (**Figure 5**), are reported in **Table S11**. The computed energetics that are not included in the main report (**Figure 5**), can be found in **Table S12.**

Table S11. Gibbs free energies of reaction (ΔG) and activation (G_A), critical bond distances at the transition states (dTS) and the magnitude of the associated imaginary frequency (IFTS). BEP estimates are reported where d_{TS} and IF_{TS} are missing.

Reaction		Surface/site	ΔG (kJ·mol^{-1})	G_A (kJ·mol^{-1})	d_{TS} (Å)	IF_{TS} (cm^{-1})
A1/D1	$CH_3CH_2COOH \longrightarrow CH_3CH_2CO + OH$	Ru	-39	68	2.14	228
		Sn/Ru	25	116	2.09	224
		SnO cluster	25	93	1.86	294
A2	$CH_3CH_2CO + H \longrightarrow CH_3CH_2CHO$	Ru	62	62	1.47	533
		Sn/Ru	81	87	1.14	100
		SnO cluster	-55	59	1.51	1274
A3	$CH_3CH_2CHO + H \longrightarrow CH_3CH_2CHOH$	Ru	44	89	1.43	1158
		Sn/Ru	21	88	1.40	1310
		SnO cluster	35	46	1.16	721
A4	$CH_3CH_2CHOH + H \longrightarrow CH_3CH_2CH_2OH$	Ru	16	80	1.46	836
		Sn/Ru	-23	61	1.59	979
		SnO cluster	-53	96	1.54	1159
		Ru-SnO	-20	71	1.50	1281
A4/B4	$OH + H \longrightarrow H_2O$	Ru	39	108	1.48	1120
		Sn/Ru	8	80	1.48	1064
		SnO cluster	62	68	1.19	763
B1	$CH_3CH_2COOH + H \longrightarrow CH_3CH_2CHOOH$	Ru	44	86	1.69	578
		Sn/Ru	64	97	1.54	538
		SnO cluster	30	142	1.39	1585
		Ru-SnO	82	82	1.46	281
B2	$CH_3CH_2CHOOH \longrightarrow CH_3CH_2CHO + OH$	Ru	-12	38	2.73	76
		Sn/Ru	42	51	2.69	108
		SnO cluster	-88	34	2.11	164
		Ru-SnO	-36	87	2.11	164
B3	$CH_3CH_2CHO + H \longrightarrow CH_3CH_2CH2O$	Ru	8	47	1.55	860
		Sn/Ru	-13	63	1.57	843
		SnO cluster	-17	151	1.45	1264
		Ru-SnO	-20	104	1.46	1425
B4	$CH_3CH_2CH_2O + H \longrightarrow CH_3CH_2CH_2OH$	Ru	49	109	1.42	1124
		Sn/Ru	36	109	1.40	1195
		SnO cluster	63	64	1.17	561
C1	$CH_3CH_2CH_2OH \longrightarrow CH_3CH_2CHOH + H$	Ru	-22	42	-	-
		Sn/Ru	6	66	-	-
		SnO cluster	61	148	-	-
C2	$CH_3CH_2CHOH \longrightarrow CH_3CH_2CH + OH$	Ru	-62	72	-	-
		Sn/Ru	-25	103	-	-
		SnO cluster	-88	46	-	-
C3	$CH_3CH_2CH + H \longrightarrow CH_3CH_2CH_2$	Ru	21	71	-	-
		Sn/Ru	32	74	-	-
		SnO cluster	-47	97	-	-
C4	$CH_3CH_2CH_2 + H \longrightarrow CH_3CH_2CH_3$	Ru	44	76	-	-
		Sn/Ru	-26	64	-	-
		SnO cluster	-12	124	-	-
D2	$CH_3CH_2CO \longrightarrow CH_3CHCO + H$	Ru	-34	22	1.49	842
		Sn/Ru	5	52	1.52	905
		SnO cluster	40	142	-	-
D3	$CH_3CHCO \longrightarrow CH_3CH + CO$	Ru	-68	65	1.79	462
		Sn/Ru	-82	84	1.95	359
		SnO cluster	61	161	-	-
E1	$CH_3CH_2COOH \longrightarrow CH_3CHCOOH + H$	Ru	-19	28	1.43	711
		Sn/Ru	26	70	1.47	927
		SnO cluster	29	137	-	-
E2	$CH_3CHCOOH \longrightarrow CH_3CCOOH + H$	Ru	-56	20	-	-
		Sn/Ru	-27	42	-	-
		SnO cluster	12	132	-	-
E3	$CH_3CCOOH \longrightarrow CH_3C + COOH$	Ru	-3	76	1.78	445
		Sn/Ru	-50	68	1.70	285
		SnO cluster	175	233	-	-

Table S12. Gibbs free energies of reaction (ΔG) and activation (G_A), critical bond distances at the transition states (d_{TS}) and the magnitude of the associated imaginary frequency (IF_{TS}). BEP estimates are reported where d_{TS} and IF_{TS} are missing. These are additional reactions not included in **Figure 5**.

Reaction		Surface/site	ΔG (kJ·mol^{-1})	G_A (kJ·mol^{-1})	d_{TS} (Å)	IF_{TS} (cm^{-1})
S1	CH3CH2COOH ⟶ CH3CH2COO + H	Ru	-90	42	-	-
		Sn/Ru	-74	50	-	-
		SnO cluster	-82	0	-	-
S2	CH3CH2COO ⟶ CH3CH2CO + O	Ru	-1	88	1.74	381
		Sn/Ru	15	154	1.79	366
		SnO cluster	79	124	2.02	266
S3	CH3CH2CO + H ⟶ CH3CH2COH	Ru	89	131	-	-
		Sn/Ru	69	122	-	-
		SnO cluster	55	55	1.17	544
S4	CH3CH2COH + H ⟶ CH3CH2CHOH	Ru	35	74	-	-
		Sn/Ru	60	78	-	-
		SnO cluster	-62	100	1.69	311
S5	O + H ⟶ OH	Ru	73	143	1.27	1332
		Sn/Ru	68	140	1.34	1317
		SnO cluster	0	46	1.25	1027
S6	CH3CH2CO ⟶ CH2CH2CO + H	Ru	9	80	1.56	938
		Sn/Ru	64	113	1.50	941
		SnO cluster	97	161	-	-
S7	CH2CH2CO ⟶ CH2CH2 + CO	Ru	-113	18	1.78	282
		Sn/Ru	-104	53	1.87	343
		SnO cluster	20	134	-	-
S8	CH3CH2CH2OH ⟶ CH3CH2CH2 + OH	Ru	-64	132	-	-
		Sn/Ru	14	193	-	-
		SnO cluster	-39	116	2.15	334
S9	CH3CH2CO --> CH3CH2 + CO	Ru	-56	80	1.96	445
		Sn/Ru	-33	98	1.95	411
		SnO cluster	62	165	-	-

Adsorption energies

In **Table S13**, we report the adsorption energies of small molecular fragments relevant to reduction on Ru, Sn/Ru, and SnO/Ru.

Table S13. Relative adsorption energies (kJ mol^{-1}) of selected molecular fragments on models in this work.

	Ru	Sn/Ru	SnO/Ru	Gas-phase reference
ΔE_{CH2}	-203	-168	-113	CH_3-1/2H_2
ΔE_{CH3}	-195	-171	-187	CH_3
ΔE_{CO}	-207	-195	-16	CO
ΔE_{H}	-66	-60	-44	1/2H_2
ΔE_{H2O}	-71	-46	-50	H_2O
ΔE_{O}	-41	-12	-2	H_2O-H_2
ΔE_{OH}	-41	2	-68	H_2O-1/2H_2

References

1. Vardon, D. R.; Settle, A. E.; Vorotnikov, V.; Menart, M. J.; Eaton, T. R.; Unocic, K. A.; Steirer, K. X.; Wood, K. N.; Cleveland, N. S.; Moyer, K. E.; Michener, W. E.; Beckham, G. T., Ru-Sn/AC for the Aqueous-Phase Reduction of Succinic Acid to 1,4-Butanediol under Continuous Process Conditions. *ACS Catal.* **2017,** *7*, 6207-6219.
2. Ratnasamy, C.; Wagner, J. P., Water Gas Shift Catalysis. *Catal. Rev.* **2009,** *51*, 325-440.
3. Kresse, G.; Hafner, J., Ab Initio Molecular Dynamics for Liquid Metals. *Phys. Rev. B* **1993,** *47*, 558-561.
4. Kresse, G.; Hafner, J., Ab Initio Molecular-Dynamics Simulation of the Liquid-Metal-Amorphous-Semiconductor Transition in Germanium. *Phys. Rev. B* **1994,** *49*, 14251-14269.
5. Kresse, G.; Furthmüller, J., Efficiency of Ab-Initio Total Energy Calculations for Metals and Semiconductors Using a Plane-Wave Basis Set. *Comput. Mater. Sci.* **1996,** *6*, 15-50.
6. Kresse, G.; Furthmüller, J., Efficient Iterative Schemes for Ab Initio Total-Energy Calculations Using a Plane-Wave Basis Set. *Phys. Rev. B* **1996,** *54*, 11169-11186.
7. Blöchl, P. E., Projector Augmented-Wave Method. *Phys. Rev. B* **1994,** *50*, 17953-17979.
8. Kresse, G.; Joubert, D., From Ultrasoft Pseudopotentials to the Projector Augmented-Wave Method. *Phys. Rev. B* **1999,** *59*, 1758-1775.
9. Perdew, J. P.; Burke, K.; Ernzerhof, M., Generalized Gradient Approximation Made Simple. *Phys. Rev. Lett.* **1996,** *77*, 3865-3868.
10. Tkatchenko, A.; Scheffler, M., Accurate Molecular Van Der Waals Interactions from Ground-State Electron Density and Free-Atom Reference Data. *Phys. Rev. Lett.* **2009,** *102*, 073005.
11. Murnaghan, F. D., The Compressibility of Media under Extreme Pressures. *PNAS* **1944,** *30*, 244-247.
12. Birch, F., Finite Elastic Strain of Cubic Crystals. *Phys. Rev.* **1947,** *71*, 809-824.
13. Makov, G.; Payne, M. C., Periodic Boundary Conditions in Ab Initio Calculations. *Phys. Rev. B* **1995,** *51*, 4014-4022.
14. Neugebauer, J.; Scheffler, M., Adsorbate-Substrate and Adsorbate-Adsorbate Interactions of Na and K Adlayers on Al(111). *Phys. Rev. B* **1992,** *46*, 16067-16080.
15. Henkelman, G.; Uberuaga, B. P.; Jónsson, H., A Climbing Image Nudged Elastic Band Method for Finding Saddle Points and Minimum Energy Paths. *J. Chem. Phys.* **2000,** *113*, 9901-9904.
16. Henkelman, G.; Jónsson, H., A Dimer Method for Finding Saddle Points on High Dimensional Potential Surfaces Using Only First Derivatives. *J. Chem. Phys.* **1999,** *111*, 7010-7022.
17. Sutton, J. E.; Vlachos, D. G., A Theoretical and Computational Analysis of Linear Free Energy Relations for the Estimation of Activation Energies. *ACS Catal.* **2012,** *2*, 1624-1634.
18. Wang, S.; Vorotnikov, V.; Sutton, J. E.; Vlachos, D. G., Brønsted–Evans–Polanyi and Transition State Scaling Relations of Furan Derivatives on Pd(111) and Their Relation to Those of Small Molecules. *ACS Catal.* **2014,** *4*, 604-612.
19. Wang, S.; Petzold, V.; Tripkovic, V.; Kleis, J.; Howalt, J. G.; Skulason, E.; Fernandez, E. M.; Hvolbaek, B.; Jones, G.; Toftelund, A.; Falsig, H.; Bjorketun, M.; Studt, F.; Abild-Pedersen, F.; Rossmeisl, J.; Norskov, J. K.; Bligaard, T., Universal Transition State Scaling Relations for (de)Hydrogenation over Transition Metals. *Phys. Chem. Chem. Phys.* **2011,** *13*, 20760-20765.
20. Wang, S.; Temel, B.; Shen, J.; Jones, G.; Grabow, L. C.; Studt, F.; Bligaard, T.; Abild-Pedersen, F.; Christensen, C. H.; Nørskov, J. K., Universal Brønsted-Evans-Polanyi Relations for C–C, C–O, C–N, N–O, N–N, and O–O Dissociation Reactions. *Catal. Lett.* **2011,** *141*, 370-373.
21. Li, M.-R.; Wang, G.-C., Differentiation of the C-O and C-C Bond Scission Mechanisms of 1-Hexadecanol on Pt(111) and Ru(0001): a First Principles Analysis. *Catal. Sci. Technol.* **2017,** *7*, 743-760.
22. Chiu, C.-c.; Genest, A.; Rösch, N., Decomposition of Ethanol Over Ru(0001): A DFT Study. *Top. Catal.* **2013,** *56*, 874-884.
23. Liu, J.; LÜ, C.; Jin, C.; Guo, Y.; Wang, G., Density Functional Theoretical Studies on the Methanol Adsorption and Decomposition on Ru(0001) Surfaces. *Chem. Res. Chin. Univ.* **2016,** *32*, 234-241.
24. Lu, J.; Faheem, M.; Behtash, S.; Heyden, A., Theoretical Investigation of the Decarboxylation and Decarbonylation Mechanism of Propanoic Acid over a Ru(0001) Model Surface. *J. Catal.* **2015,** *324*, 14-24.
25. Moura, A. S.; Fajín, J. L. C.; Pinto, A. S. S.; Mandado, M.; D. S. Cordeiro, M. N., Competitive Paths for Methanol Decomposition on Ruthenium: A DFT Study. *J. Phys. Chem. C* **2015,** *119*, 27382-27391.
26. Sutton, J. E.; Vlachos, D. G., Ethanol Activation on Closed-Packed Surfaces. *Ind. Eng. Chem. Res.* **2015,** *54*, 4213-4225.
27. Sinha, N. K.; Neurock, M., A First Principles Analysis of the Hydrogenation of C1C4 Aldehydes and Ketones over Ru(0 0 0 1). *J. Catal.* **2012,** *295*, 31-44.
28. Michel, C.; Zaffran, J.; Ruppert, A. M.; Matras-Michalska, J.; Jedrzejczyk, M.; Grams, J.; Sautet, P., Role of Water in Metal Catalyst Performance for Ketone Hydrogenation: a Joint Experimental and Theoretical Study on Levulinic Acid Conversion into Gamma-Valerolactone. *Chem. Comm.* **2014,** *50*, 12450-12453.

29. Olcay, H.; Xu, Y.; Huber, G. W., Effects of Hydrogen and Water on the Activity and Selectivity of Acetic Acid Hydrogenation on Ruthenium. *Green Chem.* **2014,** *16*, 911-924.
30. Zhang, M.; Yao, R.; Jiang, H.; Li, G.; Chen, Y., Catalytic Activity of Transition Metal Doped Cu(111) Surfaces for Ethanol Synthesis from Acetic Acid Hydrogenation: a DFT Study. *RSC Adv.* **2017,** *7*, 1443-1452.
31. Mamun, O.; Walker, E.; Faheem, M.; Bond, J. Q.; Heyden, A., Theoretical Investigation of the Hydrodeoxygenation of Levulinic Acid to γ-Valerolactone over Ru(0001). *ACS Catal.* **2017,** *7*, 215-228.
32. Mirwald, J. W.; Inderwildi, O. R., Unraveling the Fischer-Tropsch mechanism: a combined DFT and microkinetic investigation of C-C bond formation on Ru. *Phys. Chem. Chem. Phys.* **2012,** *14* (19), 7028-7031.
33. Yang, M.-L.; Zhu, J.; Zhu, Y.-A.; Sui, Z.-J.; Yu, Y.-D.; Zhou, X.-G.; Chen, D., Tuning selectivity and stability in propane dehydrogenation by shaping Pt particles: A combined experimental and DFT study. *J. Mol. Catal. A: Chem.* **2014,** *395*, 329-336.
34. Hook, A.; Massa, J. D.; Celik, F. E., Effect of Tin Coverage on Selectivity for Ethane Dehydrogenation over Platinum–Tin Alloys. *J. Phys. Chem. C* **2016,** *120*, 27307-27318.